Assembly Behavior and Thermodynamic Stability of Complex Colloidal Superstructures

by

Kwanghwi Je

A dissertation submitted in partial fulfillment
of the requirements for the degree of
Doctor of Philosophy
(Chemical Engineering)
in The University of Michigan
2023

Doctoral Committee:

Professor Sharon C. Glotzer, Chair
Associate Professor Xiaoming Mao
Professor Michael J. Solomon
Professor Robert M. Ziff

Kwanghwi Je

jekw@umich.edu

ORCID iD: 0000-0002-5017-6034

To mom and dad.

ACKNOWLEDGEMENTS

First and foremost, I would like to thank my advisor Professor Sharon Glotzer. You taught me how to do a good science, how to write a paper, how to work with others, how to learn from mistakes. Because of you, I will feel more confident wherever my next steps lead me. I would also like to thank my committee members: Professor Robert M. Ziff, Michael J. Solomon, and Xiaoming Mao for taking the time to discuss my work and keep me on the right path. Next, I should especially thank Professor Michael Engel (University of Erlangen-Nuremberg, Germany). He guided me on how to do research and science when I began my study in this group. I would like to thank Sangmin Lee and Dr.Thi Vo who provided mentorship on many different projects. I also thank Karen Coulter and Dr. Joshua A. Anderson, who have supported everything happening in this group. Lastly, I would like to thank my family and friends. Mom and Dad, thanks for supporting me throughout my graduate studies; it made my life a lot easier. I doubt I would be here without you.

TABLE OF CONTENTS

LIST OF FIGURES

Figure

LIST OF TABLES

Table

ABSTRACT

This thesis present computational studies on the self-assembly and stability of complex colloidal superstructures, including colloidal quasicrystals and polyhedron nanoparticle superlattices. The first work presents a systematic study of the growth of colloidal dodecagonal quasicrystals in systems of hard tetrahedra. Using a pattern recognition algorithm in conjunction with higher-dimensional crystallography, I analyze phason error of growing quasicrystals to follow the evolution of quasiperiodic order. I observe that the colloidal quasicrystals grow via error-and-repair mechanism; quasicrystals first grow with weak phason error and repair the error via structural rearrangements. I also observe transformation from the first order approximant to the quasicrystal via continuous phason strain relaxation. My findings demonstrate that colloidal quasicrystals can be thermodynamically stable and grow with high structural quality – just like their alloy quasicrystals counterpart.

In the second work, I investigate thermodynamic stability of model icosahedral quasicrystals against rational approximants. I construct 6 rational approximants using higher-dimensional projection, and assess the stability of those approximants against the icosahedral quasicrystals. I find in molecular dynamics simulations that 2/1 approximants and 3/2 approximants transform into the icosahedral quasicrystals, which is monitored by evolution of phason strain and diffraction pattern. This result demonstrates that the icosahedral quasicrystals are more stable than the approximants. My finding combined with collaborators' free energy calculations of compet-

ing phases demonstrates that the icosahedral quasicrystals are metastable, which is consistent with the majority of experimentally observed icosahedral quasicrystals. Using higher dimensional crystallography, I further show that the transformations of the approximants are manifested as a rotation of hypersurface in six-dimensional space. Phase transformation simulations and higher dimensional crystallography outlined in this work elucidate stability and transformation dynamics of icosahedral quasicrystals.

In the third work, I investigate the assembly behavior of polyhedral nanoparticles coated with flexible DNA ligands. Using a model constructed based on TPT calculations, I find that spatial distribution of DNA ligands on nanoparticle surface plays an important role in stabilizing complex structures of polyhedra. Considering the spatial distributions, I present coarse-grained simulation models that predict assembly behavior of polyhedron nanoparticle superlattices. In molecular dynamics simulations of the models, I observe formation of simple hexagonal, Minkowski, I-43d, and body-centered-cubic phases from DNA-coated octahedra and formation of four complex binary superlattices from binary mixtures of DNA-coated polyhedra that match with self-assembly experiments by collaborators. The assembly of four complex binary superlattices suggests that mixing DNA-coated polyhedra can serve as a powerful approach for preparing complex colloidal superstructures. My simulations and models would be useful for predicting the assembly of complex superlattices from polyhedra coated with flexible DNA.

As a whole, this thesis demonstrates how colloidal interactions originating from geometry or ligand design can have profound impact for the generation of stable complex colloidal superstructures. I anticipate that simulations and computational approaches demonstrated in the thesis offer new paradigms in understanding and

predicting assembly of complex colloidal materials.

CHAPTER I

Introduction

Nanoparticle-based complex architectures have drawn attention for decades due to their special electromagnetic[5], catalytic[6], vibration[7], and optical[8] properties. The properties of these architectures depend in part on particle properties, but more importantly on how the particles are arranged. A promising approach towards achieving complex particle arrangements is self-assembly: the self-organization of individual particles into ordered structures. Self-assembly of colloidal nanoparticles offer a powerful pathway for building complex superstructures from the bottom up, leading to novel functional materials, including metamaterials[7] and photonic crystals[8]. Yet, the structural complexity of known self-assembled colloidal superstructures has so far been limited to certain simple symmetries. The majority of colloidal nanoparticles usually assemble into densely packed crystals with simple symmetries, limiting potential applications.

Colloidal nanoparticles with anisotropic shape[9] or certain surface chemistry [10] impart complicated interparticle forces. The complicated interparticle forces can lead to complex local particle ordering, which facilitates access to crystalline phases with complex symmetries. Indeed, some nanoparticles with complicated interparticle interactions can self-assemble into clathrate colloidal crystals[11], low-symmetry

colloidal crystals[12], and Frank-Kasper colloidal crystals[13]. However, the mechanisms that lead to self-assembly of these complex superstructures from colloids remain poorly understood. Only a small number of complex colloidal superstructures have been demonstrated and it is unclear what features of the colloids contribute to their self-assembly. This lack of understanding prevents us from predicting, a priori, which structure will be assembled under which conditions, and why.

For the use of complex colloidal superstructures in practical applications, another key feature that needs to be demonstrated is the stability of the superstructures. To realistically achieve implementation in functional device, colloidal superstructures should exhibit high thermal or mechanical stability at certain thermodynamic conditions (e.g. temperature or pressure) and should be thermodynamically stable than competing phases. However, in experiment, addressing and predicting stability of superstructures are challenging tasks. Experiments may not probe the thermodynamic stability of superstructures and which feature of colloids stabilizes superstructures.

In this dissertation, I investigate the assembly behavior and thermodynamic stability of complex colloidal superstructures using molecular simulations. In Chapter 2, I begin with a brief overview of simulation methods and structural analysis methods used in these studies.

In Chapter 3, I investigated the self-assembly of colloidal quasicrystals. Quasicrystals are a unique class of ordered solids – typically metal alloys – that display complex arrangements that are ordered but not periodic [14] Quasicrystals have been discovered in a variety of materials ranging from atoms [14] to molecules [15] to colloidal nanoparticles [16]. The structural universality of quasicrystals across these very disparate systems raises one question: do quasicrystals form in a same way across all systems, regardless of building block type or size? This fundamental puzzle, the for-

mation mechanism of quasicrystal, has been clearly unraveled only in alloy systems [17]. Electron microscopy of alloy quasicrystal formation suggests that quasicrystals first grow with phason strain, a measure describing quasiperiodic disorder over long distance. Thereafter, phason strain is relaxed through local atomic rearrangements, eventually leading to a high-quality quasicrystal with negligible phason strain. While the growth process of alloy quasicrystals is well characterized, formation mechanism of colloidal quasicrystals remains elusive. Here, I study formation mechanism of colloidal quasicrystals via Monte Carlo simulations of hard tetrahedra, which are simple models for polyhedral nanoparticles that form a quasicrystal due solely to entropic forces. Specific goal of this work is to analyze phason strain during the colloidal quasicrystal growth to follow the evolution of quasiperiodic order. I observe that the colloidal quasicrystals grow via error-and-repair mechanism; the quasicrystals first grow via weak phason strain and relax the phason strain via relaxation. I also find that the quasicrystals can be more stable than the first order approximant, a periodic crystal phase competing with the colloidal quasicrystals. These results suggest that stable colloidal quasicrystals can grow with negligible phason strain, just like alloy quasicrystals. Because colloidal quasicrystals with negligible phason strain may exhibit the properties of complete photonic bandgap [18], my findings can directly benefit optical communities that focus on fabricating complete bandgap materials.

In Chapter 4, in collaboration with Engel group at the University of Nuremberg-Erlangen group, I computationally investigate the thermodynamic stability of icosahedral quasicrystals. Since the first discovery of Al_6Mn icosahedral quasicrystals [14], many icosahedral quasicrystals have been experimentally observed in alloy systems [19, 20, 21]. Including the first reported Al_6Mn icosahedral quasicrystals, many icosahedral quasicrystals were obtained by rapid solidification and metastable with

respect to periodic crystalline approximants. This raises the question of whether icosahedral quasicrystals can be thermodynamically stable over approximants. In this work, I use molecular dynamic simulations to study stability of icosahedral quasicrystals. Focus of this project is to induce structural transformations from quasicrystal approximants to icosahedral quasicrystals by annealing, which would demonstrate relative stability of icosahedral quasicrystals. I found that 2/1 approximants and 3/2 approximants transformed into icosahedral quasicrystals via continuous phason strain relaxation, indicating that icosahedral quasicrystals are more stable than the approximants. Colloborator's free energy calculations further suggest that the free energy of an icosahedral quasicrystal is higher than free energies of 1/1 approximants and other periodic crystals. These results demonstrate that icosahedral quasicrystals are metastable, just like the majority of alloy icosahedral quasicrystals. My work provides insight into the stability of icosahedral quasicrystals and suggests a practical approach for assessing relative stability of quasicrystals over quasicrystal approximants.

In Chapter 5, I explore how DNA-coated polyhedral gold nanoparticles assemble into exotic colloidal superstructures. The functionalization of polyhedral nanoparticles with DNA ligand has been an effective strategy for assembly of superlattices [10]. Yet, it remains challenging to use DNA-mediated assembly to reliably produce polyhedron nanoparticle superlattices with long-range order and a wide range of crystal symmetries. Here, in collaboration with Mirkin group at the Northwestern University, I report an approach of engineering DNA ligand flexibility towards assembly of long-range ordered polyhedron nanoparticle superlattices. In this approach, tuning ligand flexibility enable formation of superlattices with crystalline domains of up to 40 micrometers. Using a combination of experiments, simulation, and theory, the

role of flexible DNA-coating on the assembly behavior is systematically studied. The proposed approach can guide self-assembly of polyhedra into a diverse set off superlattices with well-defined crystal symmetries, including new binary superlattices with complex symmetries. This joint experimental–computational study demonstrates the power of DNA-mediated assembly and further narrows the gap between the richness of crystal structures found with atoms and in soft matter assemblies.

Lastly, I conclude in Chapter 6 with a summary and outlook for the assembly of complex colloidal superstructures.

CHAPTER II

Methods

2.1 Simulation Methods

2.1.1 Hard Particle Monte Carlo

Statistical mechanics is commonly used to calculate the macroscopic properties of a many-particle system from the collection of microscopic states of the system. Because the total number of microscopic states of a system is extremely large, sampling all microscopic states for calculating macroscopic properties is impossible or impractical. Monte Carlo simulations sample relatively small but representative microscopic states, from which estimates of macroscopic properties can be efficiently calculated [22]. In these simulations, microscopic states specified by particle configurations (positions or orientations) are randomly sampled with a relative probability proportional to the Boltzmann factor; a system in one microscopic state (μ) moves to another trial microscopic state (ν) by randomly displacing position or orientation of a randomly selected particle, and the move is accepted with a following probability.

$$\mathrm{acc}(\mu \to \nu) = \min\left(1, \frac{exp[-\beta U(\nu)]}{exp[-\beta U(\mu)]}\right) \tag{2.1}$$

where $U(i)$ is potential energy of state i and $exp[-\beta U(i)]$ is probability proportional to Boltzmann factor for state i. This simulation method ensures that the representative microscopic states are sampled according to its underlying statistical mechanical

probability distribution.

In the hard particle systems, interparticle potential energy between two hard particles h_1 and h_2 has the form

$$U(h_1, h_2) = \begin{cases} \infty & \text{if } h_1 \text{ and } h_2 \text{ overlap} \\ 0 & \text{otherwise} \end{cases} \tag{2.2}$$

Accordingly, in the hard particle Monte Carlo simulations, a trial move from a state μ to a state ν is always accepted if there is no overlap among particles in the microstate ν and the trial move is always rejected if there is one or more overlap among particles in the microstate ν:

$$\text{acc}(\mu \to \nu) = \begin{cases} min(1,1) = 1 & \text{if there is no overlap} \\ min(1,0) = 0 & \text{if there is one or more overlap} \end{cases} \tag{2.3}$$

In essence, hard particle Monte Carlo simulations sample representative microscopic configurations with no overlaps.

In chapter 3, I use hard particle Monte Carlo simulations to investigate assembly behavior of hard tetrahedron, a simple model for anisotropic colloidal particle. In those simulations, trial translation move or rotation move were attempted in each Monte Carlo cycle, and the moves were rejected if they resulted in particle overlaps. The simulations were performed with Hoomd-Blue [23] using the HPMC-plugin.[24]

2.1.2 Molecular Dynamics

Another molecular simulation method that samples microscopic states is Molecular Dynamics (MD). MD simulations produce a series of microscopic states by integrating Newton's equation of motion of model particles (atoms, molecules, or nanoparticles) in a system. Unlike Monte Carlo simulations, MD simulations provide

information of the movement trajectories of the model particles. Thus, MD simulations can be conducted to investigate macroscopic properties of a many-particle system as well as dynamical behavior of the system, such as assembly pathway of colloidal crystals.

A key element for MD simulations is the pair potential, which governs the pairwise interactions between any two model particles. Because considering all the atomistic interactions is challenging, coarse-grained models with relatively simple pair potentials are usually used to represent pairwise interactions among particles. For a spherical particle dispersion, simple isotropic pair potential that only depend on radial distance between two particles can be used to represent interparticle interactions. In contrast, for particles with anisotropic shape, it is challenging to describe effective interparticle potentials that depend on particle positions, orientations, and geometries. Rigid bodies of interacting spheres have been used to model particles with shapes [25]. However, these models require calculation of large number of pair-wise interactions and thus increase the computational cost. Recently, Vyas et al. have devised a new coarse-grained approach for modelling interactions between particles with shapes [26]. This approach can be used to generalize a wide range of force fields to account for anisotropic shape while significantly reducing the number of pair-wise interaction calculations.

In chapters 4 and 5, I investigate phase behavior of spherical nanoparticles and polyhedral nanoparticles using molecular dynamics simulations. Instead of Monte Carlo simulations that rely on random sampling, molecular dynamics simulations are used in those works to study dynamics of particle rearrangement and local particle ordering. For chapter 4, I used isotropic pair potential to represent interactions between model spherical particles. For chapter 5, I used aforementioned coarse-grained

approach by Vyas et. al [26] to model interactions between polyhedral nanoparticles. Details on the simulation models and approaches are contained in chapter 4 and 5. All simulations were perfomred with Hoomd-Blue software package [23].

2.2 Structural Analysis of Quasicrystals and Quasicrystals Approximants

The contents of this section were adapted from a publication in preparation, authored by Nydia Roxana Varela-Rosales, Kwanghwi Je, Sharon C. Glotzer, and Michael Engel, and from Ref. : "Entropic formation of a thermodynamically stable colloidal quasicrystal with negligible phason strain", Kwanghwi Je, Sangmin Lee, Erin G. Teich, Michael Engel, and Sharon C. Glotzer, *Proceedings of the National Academy of Sciences of the United States of America* (2021) [4].

Quasicrystals are a unique class of crystals that display a long-range translational order called quasiperiodicity, in which a structure cannot be described by periodic spacing of a unit cell. Quasicrystal approximants are periodic crystals with local structures similar to those found in quasicrystals. Locally, structures of quasicrystals and those of quasicrystal approximants are similar. However, due to innate periodicity, structures of quasicrystal approximants exhibit deviation from long-range quasiperiodic order, which is known as phason strain. Because quasicrystals typically form at system conditions near those of approximants, it is critical to characterize whether a crystallized phase corresponds to a quasicrystal or an approximant. For this, one needs to analyze the deviation from long-range quasiperiodic order in a crystallized phase. In this thesis, I analyze the long-range structural order in quasicrystals and approximants in the context of higher dimensional crystallography, and quantify phason strain to assess quasiperiodic order of those structures.

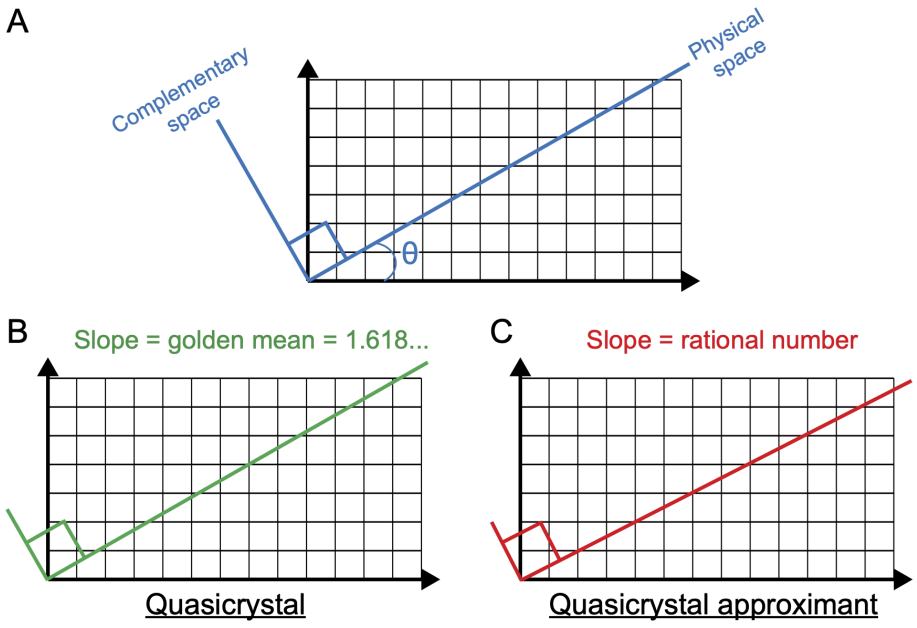

Figure 2.1: (A) A two-dimensional coordinate system defined by basis vectors of a two-dimensional square lattice is rotated with respect to a coordinate system defined by one-dimensional physical space and one-dimensional complementary space. The angle of rotation θ determines the slope between two coordinate systems. (B) If the slope between the coordinate systems is an irrational number, golden mean, projection of lattice coordinates onto physical space results in structures of one-dimensional quasicrystals. (C) If the slope between the coordinate systems is a rational number, projection of lattice coordinates leads to structures of one-dimensional quasicrystal approximant.

2.2.1 Higher Dimensional Crystallography

Structures of quasicrystals and approximants in m-dimensional physical space can be described as a projection of n-dimensional hyperlattice points onto the physical space, where $n > m$ [27, 1]. Here, the domain that contains the hyperlattice points to be projected is known as an acceptance window. In this higher dimensional crystallography description, two n-dimensional coordinate systems are introduced, where one coordinate system is rotated with respect to the other system. One coordinate system is defined by n basis vectors of a hyperlattice (Fig.2.1A). The other coordinate system is subdivided into m-dimensional physical space and (n-m)-dimensional complementary space. The slope between the two coordinate systems determines

the long-range order of projected structures. Projection with the slope of an irrational number leads to a structure with an ideal quasiperiodic order, a quasicrystal (Fig.2.1.B). Projection with a rational slope leads to a quasicrystal approximant (Fig.2.1C), and its long-range periodic order deviating from the ideal quasiperiodic order depends on the difference between the rational slope and irrational slope.

As a simple illustration of higher dimensional crystallography, I show the construction of 1-dimensional Fibonacci quasicrystals and quasicrystal approximants to the quasicrystal. Consider 1-dimensional physical space and a 2-dimensional square hyperlattice (Fig.2.2). A Fibonacci quasicrystal can be constructed by projecting square lattice points within an acceptance window (blue shaded region in Fig.2.2) onto physical space with an irrational slope, golden mean $\tau = (1+\sqrt{5})/2$ (Fig.2.2A). Projection with a rational slope leads to a rational approximant to the quasicrystal (Fig.2.2B), and the difference between the rational slope and the irrational slope τ demonstrates how periodic order in the approximant deviates from the quasicrystal (Fig.2.2C).

The higher dimensional crystallography is more than a mathematical construction - it can also be used to compare a structure (an approximant or a quasicrystal with defects) with an ideal quasicrystal and describe structural mismatches between the two structures (Fig.2.3). When structures with the structural mismatches are embedded to higher dimensional space, local structural mismatch is manifested as displacements of hyperlattice points in complementary space; hyperlattice points either move out of or into an acceptance window for an ideal quasicrystal. For such structures, because of the displacements, norm of coordinate vectors in complementary space increases along the translations in physical space (Fig.2.3B). Thus, the relationship of distance between two coordinates in physical space, $r^{\parallel}$, and the corre-

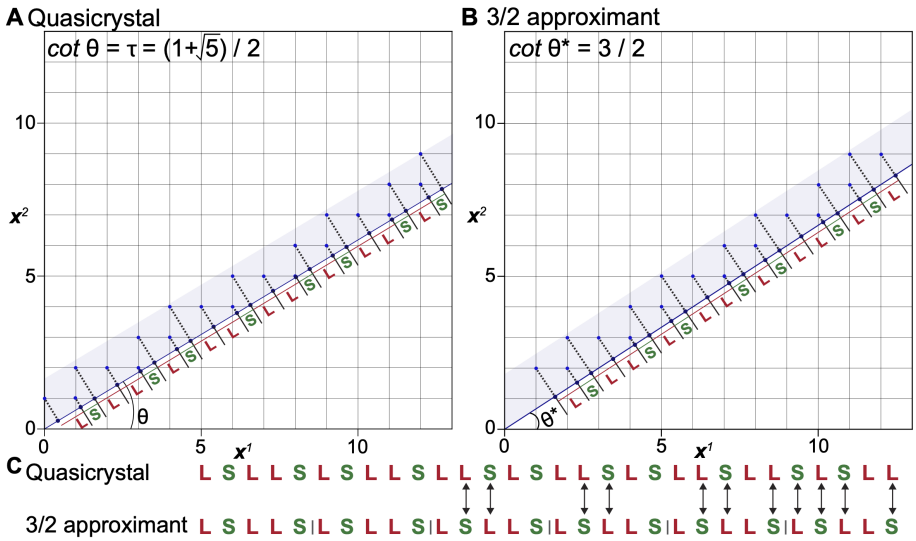

Figure 2.2: In higher dimensional crystallography [1, 2, 3], projecting a higher dimensional lattice (two-dimensional lattice with basis $\mathbf{x}^1$ and $\mathbf{x}^2$) within an acceptance window (blue shaded region) onto physical space (1-dimensional line) results in quasiperiodic or periodic structures. (A) Construction of 1-dimensional Fibonacci quasicrystal using an irrational slope, golden mean $\tau = (1 + \sqrt{5})/2$. The quasicrystal is a quasiperiodic sequence of long segment (L) and short segment (S). (B) Construction of 3/2 approximant to 1-dimensional quasicrystal using a rational slope of 3/2. The approximant is a periodic repetition of a sequence LSLLS. (C) Comparison of the constructed 3/2 approximant and the quasicrystal. Arrows represent different segments in the approximant and the quasicrystal, which correspond to local structural mismatches.

sponding distance between coordinates in complementary space, $r^{\perp}$, would describe quasiperiodic disorder over long distance [2], which is referred to as phason strain. In particular, the slope of the linear fit $r^{\perp} = \alpha r^{\parallel} + \beta$ is defined as the magnitude of phason strain [2]. In this thesis, I represent m-dimensional quasicrystals and quasicrystal approximants as m-dimensional tilings, and measured phason strain in those tilings using embedding process and phason displacement field analysis, which are detailed in the following sections 2.2.2 and 2.2.3.

2.2.2 Embedding to Higher Dimensional Space

For a tiling that can be described by higher dimensional description, all positions of tile vertices in physical space can be mapped onto higher-dimensional lattice points. This is done by mapping each tiling edge vector onto a translation vector of

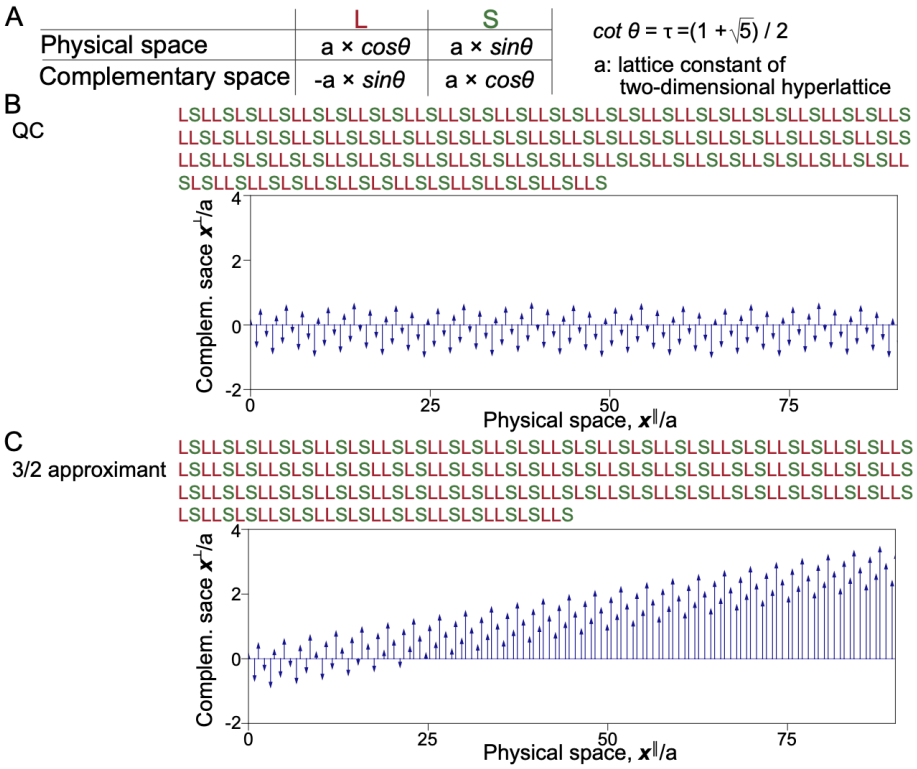

Figure 2.3: (A) Translation vectors for long segment (L) and short segment (S) in 1-dimensional physical space and 1-dimensional complementary space. (B) (top) sequence of segments L and S for a constructed 1-dimensional Fibonacci quasicrystal and (bottom) translations in complementary space and physical space calculated from the sequence. The norm of translations in complementary space are within a narrow distribution. (C) The same as in (B) but for a constructed 3/2 approximant to 1-dimensional Fibonacci quasicrystal. Because of periodicity, norm of translation in complementary space increases as a function of physical space distance.

higher dimensional lattice.

As an example, I map a dodecagonal quasicrystalline tiling in 2-dimensional physical space (Fig.2.4A) to 4-dimensional lattice. In a dodecagonal quasicrystalline tiling, all tile vertex positions are connected by twelve tiling edge vectors. The twelve tiling edge vectors are integer linear combinations of four translation vectors, e_1, e_2, e_3, and e_4 (Fig.2.3B,C). In higher dimensional crystallography, the four translation vectors can be mapped to four basis vectors of 4-dimensional lattice (Fig.2.3D). Using this mapping relation, one can map all the tiling edge vectors to translation vectors in 4-dimensional lattice, and use the translation vectors to map all vertex positions to

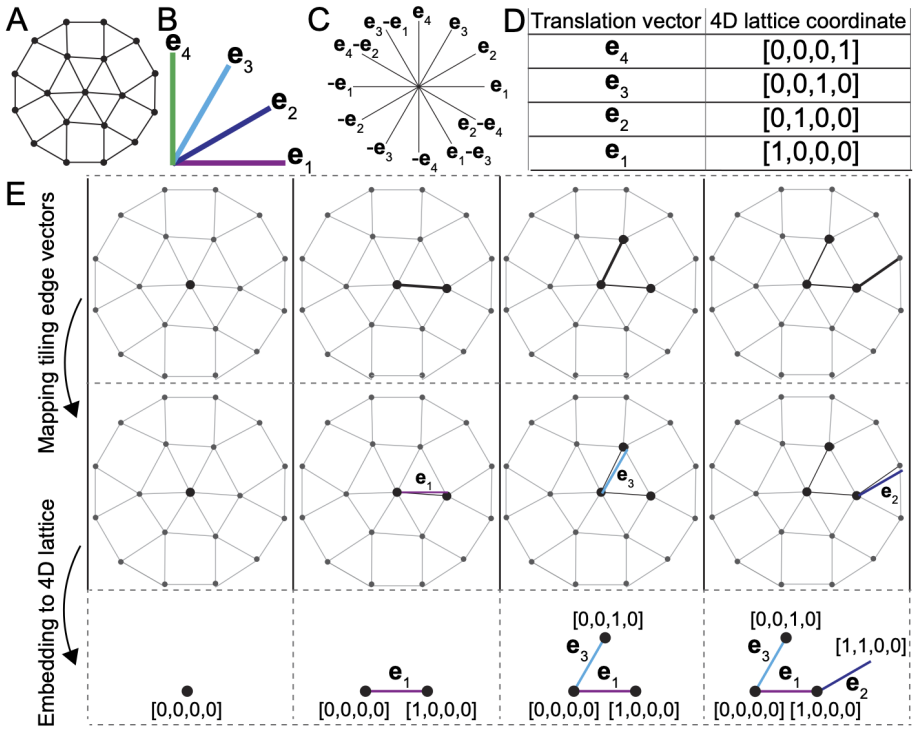

Figure 2.4: Embedding 2-dimensional dodecagonal quasicrystal tiling to 4-dimensional lattice coordinates. (A) A part of dodecagonal quasicrystal tiling. (B) Four translation vectors in two dimensional physical space. (C) The twelve possible tiling edge vectors can be mapped to integer linear combinations of these four translation vectors. (D) Mapping relation between the four translation vectors in (B) and basis vectors of four dimensional lattice. (E) I embed the tiling in (A) to 4-dimensional lattice coordinates. I first map a tiling edge vector to a linear combination of four translation vectors in (B). Thereafter, the tiling edge vector is mapped to 4-dimensional lattice translation vectors using the mapping relation in (D). By iteratively doing this mapping, one can map all the vertex position connected by tiling edge vectors to 4-dimensional lattice coordinates.

4-dimensional lattice coordinates. The step-by-step details of the mapping processes are presented below.

I start from an arbitrary vertex position and assign 4-dimensional coordinate [0,0,0,0] (Fig.2.3E, the first column). That is, the position is considered as as an origin in 4-dimensional lattice. Next, I map another vertex position that is connected with the arbitrarily selected vertex position by a tiling edge vector (Fig.2.3E, the second column, the first row). This can be done by comparing the tiling edge vector with integer linear combinations of translation vectors. By comparison, one can notice

that the tiling edge vector best aligns with translation vector e_1. Based on this comparison, I declare than the tiling edge vector corresponds to translation vector e_1 (Fig.2.3E, the second column, the second row). And based on the mapping relation in (Fig.2.3D), I assign 4-dimensional lattice coordinate [1,0,0,0] to the vertex position (Fig.2.3E, the second column, the third row).

In the same manner, I map another vertex position connected with the arbitrarily selected vertex position by a tiling edge vector (Fig.2.3E, the third column, the first row). This is done by comparing the tiling edge vector with integer linear combinations of translation vectors. By comparison, one can notice that the tiling edge vector best aligns with translation vector e_3. Based on this comparison, I declare than the tiling edge vector corresponds to translation vector e_3 (Fig.2.3E, the third column, the second row). And based on the mapping relation in (Fig.2.3D), I assign 4-dimensional lattice coordinate [0,0,1,0] to the vertex position (Fig.2.3E, the third column, the third row). By performing these comparison and lattice coordinate assignment repeatedly, one can map all the vertex positions within a tiling to 4-dimensional lattice coordinates. This procedure is usually denoted as embedding process.

2.2.3 Phason Displacement Field Analysis

After embedding, higher dimensional lattice coordinates can be projected to coordinates in physical space $r^{\parallel}$ and those in complementary space $r^{\perp}$. The following relationship concerning the average distance between two vectors in complementary space, $r_{ij}^{\perp}$, and the average distance between two vectors in physcial space, $r_{ij}^{\parallel}$ is called phason displacement:

$$r^{\perp}(r^{\perp}) = \left\langle r_{i,j}^{\perp} \middle| r_{i,j}^{\parallel} \right\rangle_{i,j} \simeq \left\langle r_{i,j}^{\perp} \middle| r_{i,j}^{\parallel} \leq r_{i,j}^{\parallel} \leq r_{i,j}^{\parallel} + \Delta r \right\rangle_{i,j} \tag{2.4}$$

The angle bracket represents averaging over all vertex pairs (i, j) with physical space distance in the interval $[r^{\parallel}_{i,j}, r^{\parallel}_{i,j} + \Delta r]$. A small interval width Δr is used for the averaging due to the discreteness of the higher dimensional lattice. Phason strain is measured as a slope of the linear fit between $r^{\perp}$ and $r^{\parallel}$ in equation (2.4).

CHAPTER III

Entropic Formation of a Thermodynamically Stable Colloidal Quasicrystal with Negligible Phason Strain

This chapter is adapted from Ref. : "Entropic formation of a thermodynamically stable colloidal quasicrystal with negligible phason strain", Kwanghwi Je, Sangmin Lee, Erin G. Teich, Michael Engel, and Sharon C. Glotzer, *Proceedings of the National Academy of Sciences of the United States of America* (2021) [4].

3.1 Introduction

Quasicrystals are crystals that possess long-range quasiperi- odic order without translational periodicity. Since the first report of an icosahedral quasicrystal in an Al–Mn alloy melt [14], quasicrystals with 8-, 10-, 12-, and 18-fold symmetry as well as icosahedral symmetry have been discovered in many alloys [28], carbon allotropes [29, 30], metal oxides [31], and various soft-matter systems including dendrimers [32], block copolymers [15, 33], and colloids [34, 35, 16, 36]. The apparent structural universality of quasi- crystals across these very disparate systems begs the question: Is quasicrystal growth the same across all systems, regardless of length scale?

How quasicrystals form is a matter of some debate [37, 38]. Two growth models have been proposed: the matching rule model and the error-and-repair model. The matching rule model [39] asserts that quasicrystals form as tiles—i.e., subunits of the

quasicrystal pattern comprising clusters of particles in specific arrangements–attach at the growth front to match the existing pattern. Matching rules dictate which attachments are allowed and which are not, and the model imagines that the tiles act as puzzle pieces with precise local fit. Via matching rules, quasi- crystals grow "perfectly," maintaining strict quasiperiodicity at all times, thereby resulting in an ideal (or perfect) tiling. In contrast, the error-and-repair model [40, 17] describes quasicrystal for- mation as a two-step process. In the first step, tiles or particle clusters quickly attach to the growing quasicrystal in a way that is at least to some degree random. These imperfect attachments eventually produce phason strain, a measure of quasiperiodic disorder over long distances [41, 42]. In the second–much slower–step, phason strain is relaxed through local particle rearrangements called phason flips. Ultimately, a quasicrystal with negligible phason strain is possible, so that the end result for both models can be very similar.

Recent in situ observations of decagonal (10-fold) quasicrystal growth from Al–Ni–Co melts using transmission electron microscopy [17] and of a self-assembling icosahedral quasicrystal using molecular dynamics simulations from a single-particle species interacting via an isotropic pair potential [2] support the error-and-repair mechanism. While these two systems, one ex- perimental and one computational, are clearly different, in both cases potential energy, rather than entropy, drives quasicrystal growth. Which growth model holds for entropically driven quasicrystal formation [43, 44, 45]? There is recent evidence that kinetic crystallization pathways in energy-dominated and entropy-dominated systems are similar [46]. Does it follow that soft-matter quasicrystals form via error-and-repair, and thus that high-quality quasicrystals are realizable in entropy-driven soft-matter systems?

In this work, I answer this question for the case of the dodecagonal quasicrystal

(DQC) in the hard tetrahedron system [47]. Because the tetrahedron particles are hard, i.e., interact only via excluded volume, the system I study is governed solely by entropy—that is, the DQC forms from entropy maximization— and thus is a good representation of a soft-matter quasicrystal. I discover from Monte Carlo (MC) simulation runs that phason strain remains small during DQC growth and only weakly relaxes further, resulting in a high-quality DQC with negligible phason strain directly from the melt. I also observe that an approximant structure, a periodic crystal closely resembling the DQC and with inherent linear phason strain [47, 48], can relax to the DQC via continuous phason strain relaxation; that is, the solid–solid transition [49, 50] occurs via a process analogous to the repair step of the error-and-repair model [40, 17].

3.2 Results

3.2.1 Tiling Hierarchy

Phason strain analysis is best performed by considering the tiling patterns for the quasicrystal under study. Fig.3.1A introduces a hierarchical series of four tilings. All tilings are generated by inflation or deflation [28] with inflation factor $f = 2cos(\pi/15) \approx 1.956$ to rescale the tile edge length. At each hierarchy level, the centers of vertex motifs (Fig.3.1B) form vertices of square, triangle, and rhombus tiles. The tiling employed in previous work [47] corresponds to the third hierarchy level (red color in Fig.3.1B), in which clusters of 22 tetrahedra are arranged in a noninterdigitating fashion; that is, the clusters do not share tetrahedra. A single 22-tetrahedron cluster (22-T) consists of a ring of 12 tetrahedra and 2 pentagonal dipyramids [47]. Phason strain in quasicrystals is quantified by numerically evaluating the geometry of the tiling. This analysis is independent of the tiling chosen within the series up to linear scaling. This means the DQC structure can in principle

be analyzed using any of the four tilings in Fig. 1. The second hierarchy level (green color in Fig.3.1B) is used in the present work.

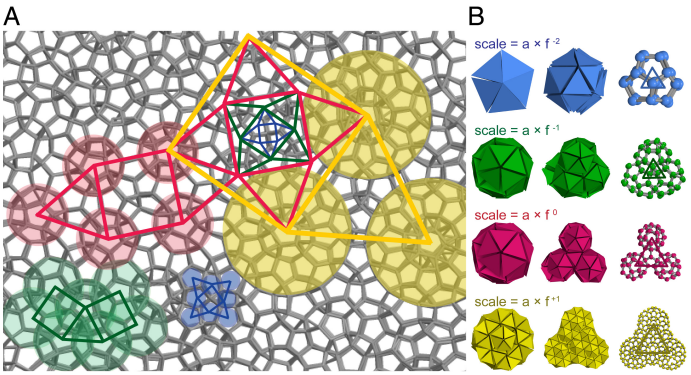

Figure 3.1: Tiling hierarchy in the DQC from hard regular tetrahedra. (A) Thick gray lines connect the centers of nearest-neighbor tetrahedra. The DQC can be described as a decorated tiling on different hierarchy levels as indicated by colors. On each hierarchy level, tile vertices are located at the centers of motifs marked by translucent colored circles. Connecting tile vertices gives square tiles, triangle tiles, and rhombus tiles arranged into a quasiperiodic tiling. Four hierarchical tilings are shown within the yellow square tile. (B) Left column: PD (blue), interdigitating 22-T (green), noninterdigitating 22-T (red), and large dodecahedral cluster (yellow) motifs. Middle and right columns: Arrangement of the motifs and relationship to the tetrahedron network for a triangle tile. In this work, I analyze the DQC using the green scale. (Image reproduced from [4])

3.2.2 Growth of the Quasicrystalline Tiling

As an initial step, I investigate the appearance of densely packed local motifs that are involved in the formation of various quasicrystals including DQCs [51, 52, 53, 54]. In dense fluid of hard tetrahedra, three local motifs have been identified: the pentagonal dipyramid (PD), icosahedron, and 22-T. I investigate the evolution of these motifs along the DQC assembly pathway obtained from an MC simulation initialized in a dense fluid phase at constant packing fraction $\phi = 0.49$ (Fig.3.2A). At this packing fraction, previous work has shown that fluid-DQC coexistence is thermodynamically preferred [47]. After 8×10^6 MC sweeps, the fraction of tetrahedra belonging to a 22-T motif significantly increases, while the fraction of tetrahedra belonging to the icosahedron and/or PD motifs only decreases. In the late stages

of the simulation, 22-T becomes the dominant motif. In parallel with this, the local density distribution gradually evolves from unimodal to bimodal by growing a second, high-density peak (Fig.3.2B). Both observations indicate that quasicrystal nucleation occurs at 8×10^6 MC sweeps and that the motif involved in nucleation and growth in the hard tetrahedron system is the 22-T.

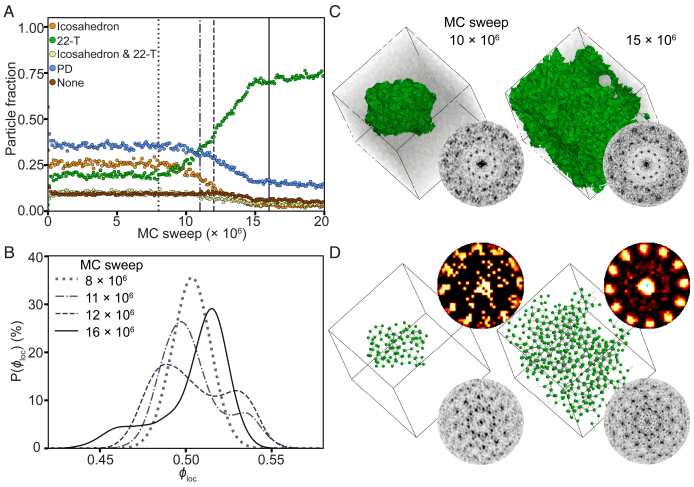

Figure 3.2: Evolution of the quasicrystalline tiling during DQC growth. (A) Fractions of tetrahedra that are part of an icosahedron, a 22-T, both an icosahedron and a 22-T, a PD but not an icosahedron or a 22-T, and none of these motifs ("None") during DQC growth. All five labels add up to 100. (B) Distribution of local density ϕ_{loc} sampled at four different MC checkpoints as marked by the four vertical lines in A. The distribution changes from unimodal to bimodal and back to mostly unimodal, indicating first the appearance and then the partial disappearance of solid–fluid coexistence. Because the simulation is conducted in the isochoric ensemble at $\phi = 0.49$, peaks shift toward lower densities as the solid grows. (C) The growing solid is identified by clustering 22-Ts that share tetrahedra as shown after 10×10^6 and 15×10^6 MC sweeps. Tetrahedra belonging to the fluid are translucent gray. Diffraction patterns of the solid (Lower Right Inset) exhibit 12-fold symmetry indicating that the solid is a DQC. (D) Networks of 22-T centers in C, which define the quasicrystalline tiling of DQC (green hierarchy level in Fig. 1). Spots in bond orientational order diagrams (Upper Right Inset) and diffraction patterns (Lower Right Inset) of the tilings gradually sharpen as DQC growth proceeds. (Image reproduced from [4])

I can obtain an intuitive picture of the contribution of 22-Ts to DQC formation by considering their spatial arrangements in the dense fluid. For this, I identify clusters of particle-sharing 22-Ts. Specifically, I track the clusters that comprise 22-Ts with six or more neighboring 22-Ts. Relatively small clusters emerge and disappear in

the fluid in the early stages of the simulation trajectory (before nucleation). After 8×10^6 MC sweeps (postnucleation), a single large cluster emerges. The diffraction pattern of the growing cluster exhibits 12-fold symmetry (Fig.3.2C), indicating that the cluster is growing as a DQC.

The 22-T motifs in the growing cluster form square, triangle, and rhombus tiles as demonstrated by the networks of 22-T centers (green solid circles) in Fig.3.2D. Diffraction patterns and bond orientational order diagrams of the 22-T centers in the growing cluster also show 12-fold symmetry with sharpening peaks, confirming that the evolving arrangements of the tiles correspond to a growing DQC tiling.

3.2.3 Analysis of Phason Strain

I calculated the phason strain in the DQC tiling during quasicrystal growth by performing a phason displacement field analysis [16, 2, 55]. For this purpose, I prepared a large DQC in a thin tetragonal box by seed-assisted growth with $N = 129,030$ hard tetrahedra. The 12-fold axis of the seed was aligned parallel to the short box axis such that growth of the 12-fold tiling proceeded laterally. I find that it is important to not restrict phason strain relaxation by periodic boundary conditions. For this reason, I performed the simulation at constant packing fraction $\phi = 0.47$, which corresponds to a density at which the DQC coexists with its fluid. In this way, the DQC does not grow into itself across periodic boundaries and is always surrounded by fluid. The contact with the fluid allows the quasicrystal to continuously relax its phason strain and reach thermodynamic equilibrium.

For the phason displacement analysis, each vertex $\mathbf{a}_m$ of the two-dimensional (2D) tiling is assigned to a point in a four-dimensional (4D) configurational space by a lifting procedure. The lifted 4D point is then projected onto the phonon-corrected position of the vertex $\mathbf{a}_m^{\parallel}$ in 2D parallel space and a coordinate in 2D

perpendicular space $\mathbf{a}_m^\perp$ that encodes phason displacement [27]. The relationship of the distance between two tile vertices in parallel space, $r_{mn}^\parallel = |\mathbf{a}_m^\parallel - \mathbf{a}_n^\parallel|$, and the corresponding distance in perpendicular space, $r_{mn}^\perp = |\mathbf{a}_m^\perp - \mathbf{a}_n^\perp|$ characterizes phason strain and is defined as the phason displacement [55]. In particular, the slope α of the linear fit, $r^\perp = \alpha r^\parallel + \beta$ is known as the phason strain [56]. I calculate α after removing background noise and scale α by the value of phason strain in the first-order approximant [47, 48] α_{1st}.

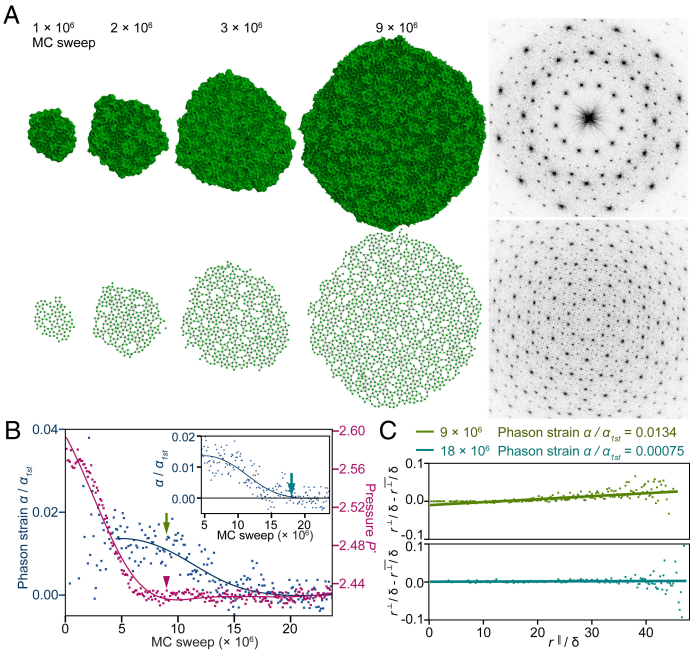

Figure 3.3: Phason strain analysis during DQC growth starting from the hard tetrahedron fluid. (A) The growing DQC solid (Upper Row) and its tiling (Lower Row). Diffraction patterns at 9×10^6 MC sweeps for tetrahedron centers (Upper Right) and tiling vertices (Lower Right) show many peaks with 12-fold symmetry, indicating a well-formed quasicrystal. (B) Evolution of system pressure P^* (magenta) and phason strain α measured from the tiling (blue). The tiling size is large enough to measure phason strain reliably after 4.5×10^6 MC sweeps (start of interpolation). Pressure converges after 9×10^6 MC sweeps (magenta arrow). Phason strain converges more slowly after 18×10^6 MC sweeps (Inset). (C) Phason displacement field analysis at the times when pressure (green) and phason strain (cyan) each converge to equilibrium values. Here, the times are marked by green and cyan arrows in B, respectively. Phason displacement is the average perpendicular space distance $r^\perp/\delta$ as a function of parallel space distance $r^\parallel/\delta$, where δ is the tile edge length. Phason displacement grows linearly. The slope of this growth is the phason strain α, which is measured from $r^\perp(r^\parallel)/\delta$ after removing background noise $\overline{r^\perp}(r^\parallel)/\delta$ and is scaled by phason strain of the first-order approximant α_{1st}. (Image reproduced from [4])

Fig.3.3A shows a growing DQC (first row) and its corresponding quasicrystalline tiling (second row). DQC growth is complete after approximately 8×10^6 sweeps, which is reflected in the convergence of the reduced pressure $P^* = P/k_BT$ (magenta arrowhead in Fig.3.3B) and that of the fraction of particles belonging to the solid. At 9×10^6 sweeps, the phason strain is $\alpha/\alpha_{1st} = 0.013$ (green arrow in Fig.3.3B and C), which is comparable to the phason strain in the third-order approximant of the DQC [47], $\alpha_{3rd}/\alpha_{1st} = 0.010$. The phason strain then gradually decreases, becoming negligible (zero) at around 18×10^6 MC sweeps (cyan arrow in Fig.3.3.B and C). These results demonstrate that only weak phason strain is introduced during growth and subsequent relaxation eventually results in a high-quality DQC with negligible phason strain and weak equilibrium phason fluctuations. I confirm formation of high-quality DQCs with negligible phason strain in three independent simulations. Next, I show that the observed phason relaxation can even occur in quasicrystal approximants with inherent phason strain, which demonstrates thermodynamic stability of DQCs over the approximants.

3.2.4 Transformation of the First-order Approximant

Quasicrystal approximants are characterized by linear phason strain [1]. Lower free energy of the quasicrystal compared to its approximants is a pre- requisite for thermodynamic stability of the quasicrystal and has thus been investigated in both experiment [20] and simulation [57]. Specifically, the first-order DQC approximant was tested for relative stability with respect to DQC in the hard tetrahedron system [48]. Equations of state demonstrated that the first-order approximant is more densely packed than both the DQC and higher- order approximants [48]. These results suggested that the first- order approximant is the thermodynamically stable phase. But, no tests of its stability have been reported.

I revisited the stability of the DQC by initializing a simulation from the first-order approximant [47, 48] in a tetragonal box at packing fraction $\phi = 0.47$. I now find that the approximant gradually transforms into the DQC. This is demonstrated by the evolution of the diffraction pattern from 4-fold symmetry to 12-fold symmetry (Fig.3.4A). The transformation is also observed at a lower packing fraction $\phi = 0.46$. These results indicate that the DQC is thermodynamically more stable than approximants at these packing fractions. I confirmed that the geometry of the simulation box does not affect the transformation.

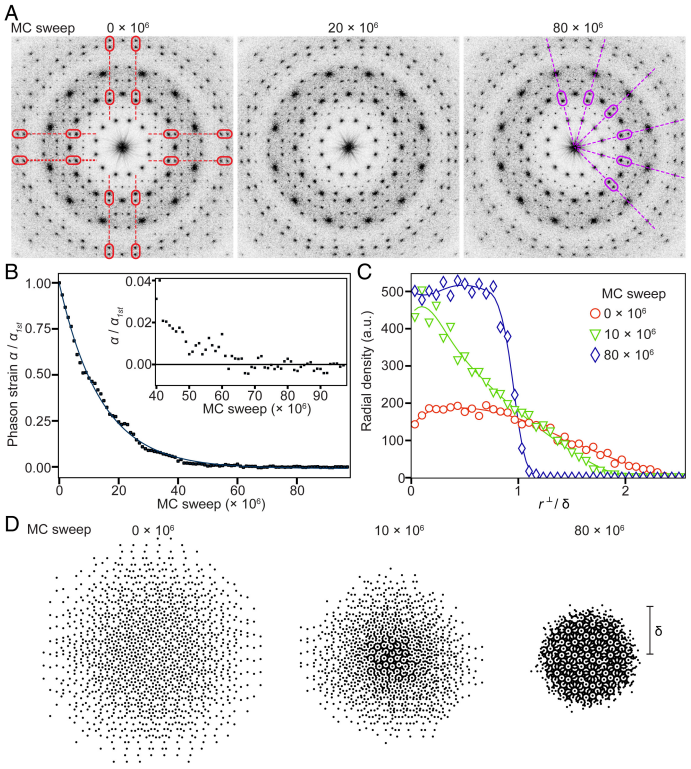

Figure 3.4: Continuous transformation from the first-order approximant to the DQC during a long MC simulation. (A) Evolution of the diffraction pattern from fourfold symmetry in the approximant (0×10^6 MC sweeps) to 12-fold symmetry in the DQC (80×10^6 MC sweeps). (B) Phason strain α/α_{1st} gradually relaxes to zero during the transformation. (C) Radial density in perpendicular space $r^{\perp}$ sharpens over time toward a compact occupation domain as expected for a high-quality DQC. (D) Snapshots of projected tile vertices in the perpendicular space sampled at 0×10^6, 10×10^6, and 80×10^6 MC sweeps. When the transformation is complete (80×10^6 MC sweeps), the positions form a single roughly circular domain with radius δ, where δ is the tile edge length. Due to random phason fluctuations, the boundary of the domain is blurred. (Image reproduced from [4])

I calculated phason strain during the transformation using the phason displacement field analysis. The phason strain decays exponentially as $\alpha/\alpha_{1st} \propto \exp -t/t_0$ with $t_0 = 14 \times 10^6$ as a function of MC sweeps t. Phason strain is zero within fluctuations after $t = 80 \times 10^6$ (Fig.3.4B). Both types of simulations, growth from the fluid and transformation of the approximant, converge to a high-quality DQC free of phason strain, demonstrating unambiguously the thermodynamic stability of the DQC. This is an observation of a transformation from an approximant to a quasicrystal in a three-dimensional (3D) simulation and the demonstration of thermodynamic stability of a simulated DQC in 3D. My observation is in line with previous simulation reports of entropically stabilized dodecagonal or decagonal quasicrystals in 2D [57, 58, 59].

Relaxation of phason strain requires coherent phason flips within the tiling. I analyzed the enhancement of structural quality of the tiling by following the evolution of the spatial distribution of tile vertices projected to perpendicular space. This distribution is known as the occupation domain. It is a polygonal domain with sharp boundaries for an ideal dodecagonal tiling with shield tiles, a spherical domain blurred out near the boundary in the case of a random tiling, and a noncompact domain in the case of an approximant [55]. During transformation from the approximant to the DQC, the radial density of projected points in perpendicular space gradually sharpens (Fig.3.4C and D), showing improvement in the structural quality of the tiling. The occupation domain remains blurred near the boundary, indicating that the DQC permits weak random phason fluctuations in equilibrium.

3.3 Discussion

Since 2004 a growing number of colloidal quasicrystals have been reported [32, 15, 33, 34, 35, 16, 36], including a quasicrystal comprising tetrahedron-shaped nanoparticles [60]. But, the quasicrystals in these systems are characterized by relatively low structural quality when compared to that of classic examples of quasicrystals of atomic alloys [28, 21]. This leads to the question of whether soft-matter quasicrystals are necessarily of inferior structural quality. The purely entropic hard tetrahedron system studied in this paper can be considered a soft-matter system because the particles interact weakly (i.e., not at all) compared to atoms. My observation of the formation of high-quality DQCs with negligible phason strain demonstrates that soft-matter quasicrystals can indeed exhibit a high degree of quasiperiodic order comparable to their alloy counterparts. My work also reveals a potential limiting factor toward quasicrystals with high structural quality: the need to anneal the quasicrystal long enough to heal out phason strain and other defects created initially during rapid growth. Atoms in alloys move orders of magnitude faster than the much more massive colloids, which explains why annealing is less of an issue in traditional QCs. Future work should search for formation modes that lead to soft-matter quasicrystals with few defects [61] or defects that heal quickly. Those soft-matter quasicrystals will be the best candidates for functional materials, e.g., complete photonic bandgap materials for next-generation optical devices [18, 62] made via self-assembly.

3.4 Methods and Supporting Information

3.4.1 Particle Geometry

A tetrahedron is the convex hull of the four vertices $v_1 = (1, 1, 1)$, $v_2 = (1, -1, -1)$, $v_3 = (-1, 1, -1)$, $v_4 = (-1, -1, 1)$. Edge length and volume of the tetrahedra are

$\sigma = 2\sqrt{2}$ and $V = 8/3$, respectively.

3.4.2 Simulation Code

Simulations were performed with the hard-particle MC (HPMC) [23] simulation code implemented in the HOOMD-blue software package, version 2.4.2 [24]. I used HPMC on multiple central processing units (CPUs) with message passing interface domain decomposition or on a single graphics processing unit at XSEDE [63]. All simulations were performed in the isochoric ensemble with periodic boundary conditions. The open-source analysis package freud [64] was used to detect motifs via pattern recognition and to quantify the local density distribution of tetrahedra.

3.4.3 Self-Assembly Simulation

Simulations were started from a fluid of 16,384 hard tetrahedra at low density, compressed to either packing fraction $\phi = 0.49$ or $\phi = 0.52$, and run for 20×10^6 MC sweeps.

3.4.4 Analysis of Local Motifs

Positions and orientations of tetrahedra were averaged over short trajectories to reduce noise. Icosahedron and 22-T motifs were detected by grouping and vector displacement analysis. In the grouping analysis, tetrahedron vertices within distance cutoff 0.3σ were grouped. The clusters of tetrahedra containing groups of size 20 and 22 vertices are candidates for icosahedron and 22-T motifs, respectively. Subsequently, in the vector displacement analysis, I created the set of vectors connecting the center of a candidate cluster to the centers of the tetrahedra in the candidate cluster. If the angular displacements between the vector set of the candidate cluster and that of the ideal motif was lower than a threshold, the candidate motif was successfully identified with the ideal motif. Detection of PDs was performed analogously

with the difference that tetrahedron edge centers instead of vertices were grouped. Local packing fraction of a tetrahedron ϕ_{loc} is defined as the packing fraction around the tetrahedron within a sphere of radius 1.77σ. The local density distribution is the histogram of local packing fractions.

3.4.5 Seed-Assisted DQC Growth (Approximant-to-DQC Transformation) Simulations

The simulation was started from a fluid prepared by placing 129,600 (136,000) hard, regular tetrahedra at low density in a thin tetragonal simulation box and compressing the system to $\phi = 0.46$. A static seed of 546 (50,324) hard tetrahedra was placed with the 12-fold axis of the seed pointed along the thin box dimension and all overlapping hard tetrahedra of the fluid removed. The simulation box was then compressed to $\phi = 0.47$. The final box dimension was $69.3\sigma \times 6.71\sigma \times 69.3\sigma$ ($70.97\sigma \times 6.71\sigma \times 70.97\sigma$). The HPMC simulation was run for 23×10^6 (95×10^6) MC sweeps with the seed immobilized for about 10^6 MC sweeps and then released. In the seed-assisted growth simulation, the DQC grows primarily in the quasiperiodic plane perpendicular to the short box axis. This approach grows a large DQC in reasonable computation time, a prerequisite to study the evolution of phason strain during the growth process. I confirmed that the short box axis does not significantly affect growth of the DQC at $\phi = 0.47$ by performing simulations in boxes with various thicknesses.

3.4.6 Tiling Determination for Phason Strain Analysis

Samples were quickly compressed to $\phi = 0.64$ to remove structural noise. The DQC was set as the seed-containing tetrahedron cluster with local densities $\phi_{loc} > 0.68$. The approximant was set as the largest tetrahedron cluster with local densities $\phi_{loc} > 0.68$. A 2D tiling with edge length δ was obtained by projecting the centers of

interdigitating 22-T motifs onto the plane perpendicular to the 12-fold axis. Because my DQC primarily grows in the 2D quasiperiodic plane, the DQC is well described by a 2D tiling. Radial density of particle positions in perpendicular space was obtained by measuring number density in concentric rings around the center of mass.

CHAPTER IV

On the Stability of a Model Icosahedral Quasicrystal and its Rational Approximants

The contents of this chapter were adapted from a publication in preparation, authored by Nydia Roxana Varela-Rosales, Kwanghwi Je, Sharon C. Glotzer, and Michael Engel. This is a collaborative work with the Engel's group at the University of Erlangen-Nuremberg. My collaborators in the Engel group performed all the free energy calculations (mostly just alluded to in the text). My major contribution to this work is performing phase transformation simulation of rational approximants to icosahedral quasicrystals and analyzing transformation simulation trajectories.

4.1 Introduction

Quasicrystals are materials that exhibit long-range order with no translational periodicity. Since the first discovery of Al_6Mn icosahedral quasicrystals (IQCs) [14], IQCs have been observed in more than 70 different metallic alloys [19]. Now, structure and symmetry of icosahedral quasicrystals are well understood. However, the stability of IQCs agasint rational approximants remains elusive. To examine the relative stability of IQCs against approximants, free energies of the competing phases need to be evaluated accurately. However, calculating free energy of an IQC is not straightforward because there is no obvious reference state from which thermody-

namic integration can be performed. For IQCs with random tiling, free energy calculation is further complicated by the fact that there is no robust way to sample all the distinct random configurations of quasicrystals to account for its configurational entropy. Kiselev et al., estimated the free energies of decagonal quasicrystals by combining configurational contribution based on the approximation of uncorrelated phason flips and phonon contribution from a quasicrystal configuration with thermodynamic integration [58]. Building on this work, Nydia Roxana Varela-Rosales in Engel group and I present a systematic approach for examining relative stability of a model IQC over their rational approximants. Nydia Roxana Varela-Rosales estimated free energies of icsoahedral quasicrystals and their rational approximants using a special variant of the technique proposed by Kieselev. Using molecular dynamics simulations, I anneal rational approximants to induce structural transformations from the approximants to IQCs. During the annealing simulation, I analyzed phason strain to follow the formation of quasiperiodic order. I observe that 2/1 approximants and 3/2 approximants transformed into IQCs via continuous phason strain relaxation, indicating that IQCs are more stable than the two approximants. Nydia's free energy calculations further show that free energy of an IQC is higher than the free energies of 1/1 approximants and BC8 crystals. These results suggest that IQC metastable, which matches with many icosehadral quasicrystals obtained by rapid cooling [21] The free energy calculation methods, phase transformation simulations, and phason analysis outlined in this work provide insight about the stability of IQCs and would be applicable to the study of stability of quasicrystals with other forbidden rotation symmetries.

4.2 Results

4.2.1 The Structure of Quasicrystals and Their Crystalline Approximants.

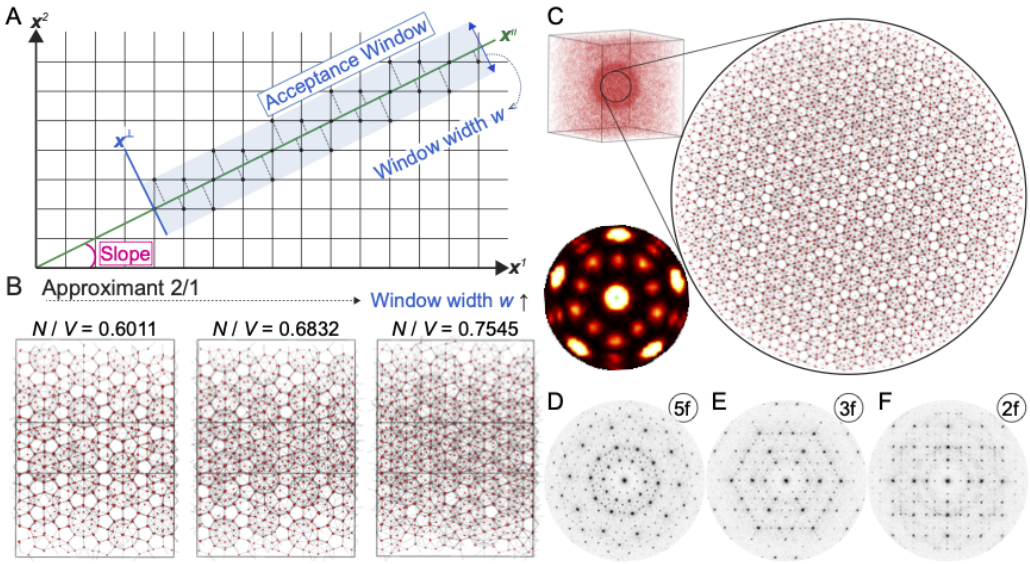

Figure 4.1: (A) Construction of rational approximants. In this construction, all sites in the higher dimensional lattice (two-dimensional square lattice) within an acceptance window (blue shaded area) are projected onto real space $\mathbf{x}^{\parallel}$. The width of the window, w, in complementary space $\mathbf{x}^{\perp}$ determines the set of lattice points to be projected. The slope between $\mathbf{x}^{\parallel}$ and the lattice determines long-range order of the projected structure. (B) Relaxed 2/1 approximants to icosahedral quasicrystals (IQCs). From left to right, the window widths used in construction and number density N/V increase. (C) Self-assembly of an icosahedral quasicrystal (IQC) in a molecular dynamics (MD) simulation. Isotropic particles form a roughly spherical IQC (right panel) that coexists with the gas phase (upper left panel). BOD of the IQC shows five-fold symmetry (lower left panel). (D-F) Diffraction patterns of the IQC in (C) along five-fold (D), three-fold (E) and two-fold (F) axes.

To study the phase stability of IQCs and their approximants, I prepared configurations of the competing phases in a model system of particles interacting via a pair potential (Materials and Methods). For approximants to IQC, I first constructed a series of rational approximants by projecting a 6-dimensional (6D) hyperlattice with body-centered-cubic symmetry onto 3-dimensional (3D) physical space. In the construction, I used rational slopes of 1/1, 12/10, 4/3, 14/10, 3/2, 8/5, 5/3, 18/10, and 2/1, and a range of acceptance window widths w (Fig.4.1A). Upon construc-

tion, each rational approximant was relaxed using NPT simulations (Materials and Methods) (Fig.4.1B). I label these relaxed rational approximants by phason strain and particle number density N/V, where N is the number of particles and V is the volume of simulation box. Configurations of IQCs were obtained from self-assembly simulations (Materials and Methods), as described in the literature [2]. Fig.4.1C-F show a typical configuration of a self-assembled IQC and its diffraction patterns. I compare stability of self-assembled IQCs to the relaxed rational approximants.

4.2.2 Probing Phase Stability by Free Energy Calculations.

Nydia Roxana Varela-Rosales estimated the free energies of IQCs and rational approximants to examine the relative stability of IQCs. Nydia Roxana Varela-Rosales's free energy calculations suggest that IQCs are more stable than approximants with phason strain $\alpha \simeq 0.0213$ and $\alpha \simeq 0.00372$ (approximants constructed with slopes 2/1 and 3/2) but less stable than the approximant with phason strain $\alpha \simeq 0.04251$ (approximant constructed with slope 12/10). These results indicate that IQCs are metastable structures.

4.2.3 Transformations of Approximants.

I now study phase transformations of approximants to verify the free energy calculations. Phase transformations from approximants to quasicrystals are not only of interest for the study of phase stability, but also have implications for understanding the formation of quasiperiodic structures from incompatible periodic crystals. Within the context of higher dimensional crystallography, a transformation of a rational approximant into a quasicrystal involves a global change of physical space orientation [3]. Analyzing the phase transformations would enable the characterization of structural evolution within higher dimensional space in which the competing

structures are embedded.

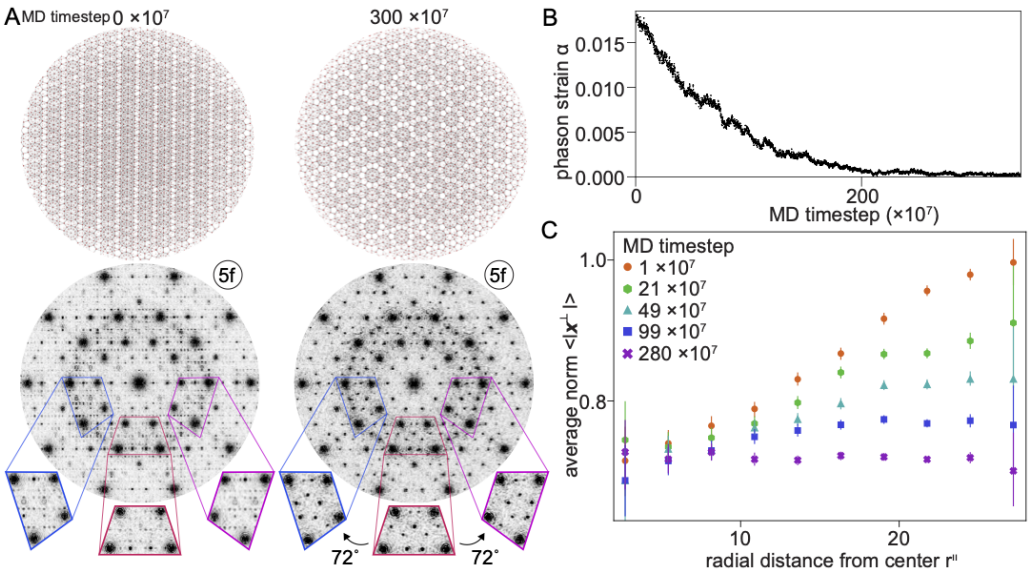

Figure 4.2: (A) Transformation from a relaxed approximant with phason strain $\alpha \simeq 0.0213$ (approximant constructed with a slope 2/1) (left) to the IQC (right) during a long MD simulation. Spherical solid (upper row) and diffraction pattern (lower row) exhibit five-fold symmetry after the transformation. (B) Phason strain gradually relaxes towards zero during the transformation. (C) Average norm of coordinates in complementary space $\mathbf{x}^{\perp}$ as a function of radial distance in physical space $r^{\parallel}$ for different MD timesteps. As a function of the radial distance, the vector norm shows an approximately linear trend.

I study the phase transformation of a relaxed approximant with phason strain $\alpha \simeq 0.0213$ (approximant constructed with a slope 2/1) and demonstrate its structural evolution. Nydia Roxana Varela-Rosales's calculation suggest that free energy of this approximant is higher than that of an IQC. I initialized a simulation of the approximant in a cubic simulation box at number density $N/V = 0.092$ and temperature $k_BT/\epsilon = 0.25$. I find that the approximant gradually transforms into the IQC (Fig.4.2A). This is demonstrated by the evolution of diffraction pattern exhibiting 5-fold symmetry after a long simulation (Fig.4.2A). This result indicates that the IQC is thermodynamically more stable than the approximant, which matches with free energy calculations by Nydia Roxana Varela-Rosales. To follow the formation of quasiperiodic structures during the transformation, I investigated the evolution of

phason strain. The phason strain decays exponentially as a function of MD timesteps and becomes $\alpha \simeq 0.000058$ within fluctuation in the final stage of the simulation (Fig.4.2B). The small but finite amount of phason strain in the IQC can be ascribed to disorder within gas/solid interface or random phason fluctuations [56] under high system temperature.

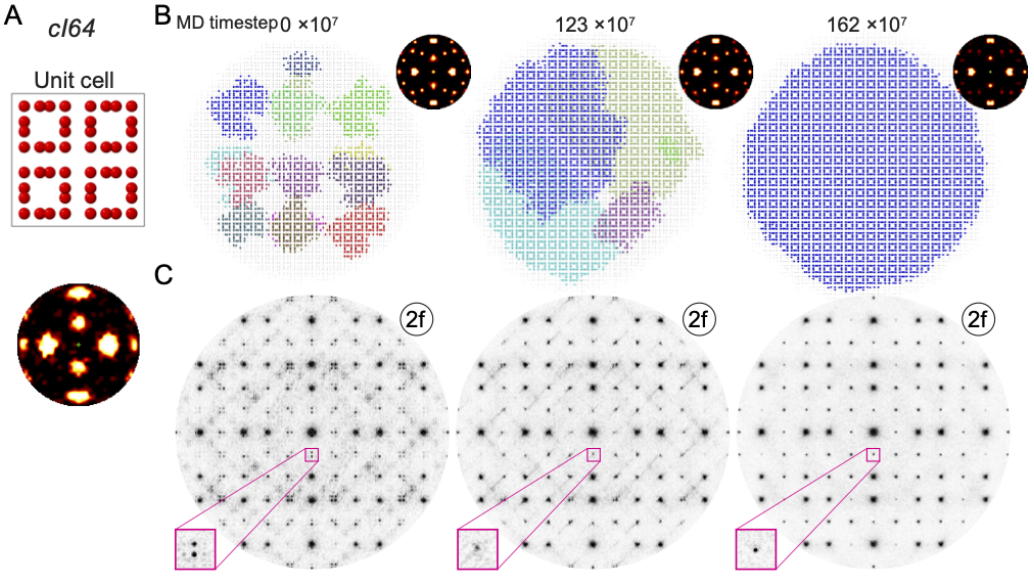

Figure 4.3: Phase transformation of a relaxed approximant with phason strain $\alpha \simeq 0.04251$ (approximant constructed with slope 12/10). (A) $cI64$ is a cubic crystal with 64 particles in a unit cell (top). Bottom panel shows a BOD of the simulated $cI64$ crystal. (B) Spherical solid and BOD along the transformation of the approximant. I show particles identified as $cI64$ crystal in large, color-coded spheres. Different colors represent different $cI64$ crystal grains in the solids. (C) Diffraction patterns of the solids in (B) viewed along a two-fold axis. The diffraction pattern from the solid in the starting frame exhibits the splitting of Bragg peaks (inset).

Relaxation of phason strain requires collective particle rearrangements within the approximant. I analyzed the collective rearrangements in a scenario where a structure is embedded in a higher dimensional space. I measured the vector norm of coordinates in complementary space as a function of a radial distance in physical space for different MD timesteps (Fig.4.2C). I find approximately linear trends between the norm and radial distance, as expected from higher dimensional crystallography

[28]. During the transformation from the approximant to the IQC, the linear trend, by and large, rotated. After transformation is complete, the norms of coordinates in complementary space lie within a narrow distribution similar to that for a constructed IQC. Since the rotation of linear trend represents a rotation of physical space with respect to 6D hyperlattice, this result provides structural description of how collective rearrangements leading to the phase transformation is manifested in higher dimensional space.

Next, I investigated the transformation of a relaxed approximant with phason strain $\alpha \simeq 0.04251$ (approximant constructed with a slope 12/10). Nydia Roxana Varela-Rosales's calculation suggest that free energy of this approximant is lower than that of an IQC. I find that this approximant transformed into a new type of a periodic crystal, $cI64$ (Fig.4.3A), a structure that is locally similar to IQC but is not classified as rational approximants. Interestingly, this transformation process was different from the previous transformation resulting in an IQC. In the parent approximant phase, a few $cI64$ crystal grains already exist (Fig.4.3B, left), as indicated by the splitting of Bragg peaks in diffraction pattern (Fig.4.3C lower left inset). These domains competitively grew along the simulation, eventually leading to a single large grain (Fig.4.3B, right). Self-assembly of IQCs, approximant-to-IQC transformations, and approximant-to-crystal transformations together demonstrate the complexity in free energy landscape for the selected model particles. I note that $cI64$ is energetically more stable than this approximant or IQC (Fig.4.4) but is less stable than a $BC8$ crystal reported in literature (Fig.4.4) [2].

4.3 Discussion and Conclusion

Since the first report of Al-Mn IQCs [14], many icosahedral quasicrystals have been reported in rapidly cooled alloys [20, 21]. Recently, IQCs are even discovered in model colloidal systems [65]. These reports have been posing an intriguing question on the thermodynamic stability of IQCs. The current work presents a systematic approach to address the stability of IQCs. Using phase transformation simulations, I study stability of a self-assembled IQC against rational approximants and other closely related periodic crystals. Consistent with the majority of experimentally observed IQCs obtained from rapid cooling [20, 21], the self-assembled IQCs are metastable.

The higher dimensional crystallography illustrated in this work serve as a powerful tool for preparing approximants for stability analysis and interpreting the evolution of quasiperiodic order. Engel group's free energy calculations illuminate the origin of stability and the respective roles of potential energy and entropy in stabilizing competing phases. The free energy calculation techniques, phase transformations, and higher dimensional crystallography outlined in this work may provide a comprehensive picture of IQC formation and stability. This approach may be applicable to a wide range of systems in which transformations between quasicrystals and periodic crystals are observed [49].

4.4 Methods and Supporting Information

4.4.1 Simulation Codes.

I performed MD simulations with the HOOMD-Blue simulation package [24] to study phase stability and transformations in systems of particles interacting via

oscillating pair potential (OPP):

$$V_{OPP}(r_{ij}) = \epsilon \left[\frac{1}{r_{ij}^{15}} + \frac{1}{r_{ij}^{3}} \cos\left(7.25(r_{ij} - 1.25) - 0.50\right) \right] \tag{4.1}$$

The quantity V_{OPP} is the potential energy of interaction between two particles i and j at a distance of r_{ij}. The unit of energy is ϵ, which is set to 1 throughout this work. The potential is truncated and shifted to zero at the local maximum following the third attractive well. All simulations were carried in a cuboid simulation box with periodic boundary conditions, using multiple central processing units (CPUs) with message passing interface domain decomposition or on a single graphics processing unit at XSEDE [63].

4.4.2 Analysis and Phase Identifications.

To correct for the rotation and translation of the quasicrystals and approximants, solids are centered in the middle of simulation box and oriented along high-symmetry axes. The open-source analysis package freud [64] was used to detect particles that are part of $cI64$ crystals and to lift particles into six-dimensional space (SI Appendix). To identify the crystal structures obtained from simulations, I use diffraction patterns and bond orientational order diagrams (BODs) of particles. The diffraction patterns are calculated by projecting particles into planes along high-symmetry axes and applying Fast Fourier Transform to the projected particles. BODs show a stereographic projection of the first nearest-neighbor bonds along high-symmetry axes.

4.4.3 Self-assembly Simulations.

I use NVT simulations for the self-assembly of IQCs. Simulations are started from a gas of $N = 144{,}000$ particles at number density 0.092, corresponding effectively to zero pressure. The temperature is linearly cooled from $k_BT/\epsilon = 0.25$ to $k_BT/\epsilon = 0.21$ over 2×10^7 MD steps to induce nucleation of IQCs. After the nucleation, the

temperature is linearly increased from $k_BT/\epsilon = 0.21$ to $k_BT/\epsilon = 0.25$ over 2×10^7 MD steps. Thereafter, I anneal systems at $k_BT/\epsilon = 0.25$ over 4×10^8 MD steps to heal defects.

4.4.4 Relaxation Simulations of Constructed Rational Approximants.

Prior to relaxation simulations, Brownian dynamics simulations are applied to the constructed rational approximants for short 2000 MD timesteps to prevent simulation blow-up, arising from some particles within unphysically short interparticle distance. I relax rational approximants using NPT integrator with zero pressure and temperature $k_BT/\epsilon = 0.25$.

4.4.5 Phase Transformation Simulations.

To study phase transformations of approximants, I perform NVT simulations of N = 144,000 particles. Each simulation is prepared by placing an approximant of 48,000 particles in gas of 96,000 particles. Number density of system is kept constant as 0.092 for all systems. The system is annealed at temperature $k_BT/\epsilon = 0.25$ for about 10^9 MD timesteps or more to promote phase transformations. Each dumped snapshot is quenched to zero temperature to remove phonon motion.

4.4.6 Higher Dimensional Crystallography - embedding and Projection

Details of the embedding and projection processes are provided in the supplementary information of literature [2]. Precise definitions and further details can be found in the literature [27, 28]. I can embed the particle positions of an IQC to a 6-dimensional hyperlattice using six 5-fold translation vectors $\mathbf{b}_j^5$ (j=1,2,...,6) and ten 3-fold translation vectors $\mathbf{b}_j^3$ (j=1,2,...,10). Six 5-fold translation vectors within icosahedral constellation in the quasicrystal are identified and mapped onto the six basis vectors of the 6-dimensional lattice listed in Table 4.1.

5-fold translation vectors	Coordinates of the 6-dimensional lattice
$\mathbf{b}_1^5 = (0, \tau, 1)$	(1,0,0,0,0,0)
$\mathbf{b}_2^5 = (\tau, 1, 0)$	(0,1,0,0,0,0)
$\mathbf{b}_3^5 = (1, 0, \tau)$	(0,0,1,0,0,0)
$\mathbf{b}_4^5 = (0, -\tau, 1)$	(0,0,0,1,0,0)
$\mathbf{b}_5^5 = (-\tau, 1, 0)$	(0,0,0,0,1,0)
$\mathbf{b}_6^5 = (1, 0, -\tau)$	(0,0,0,0,0,1)

Table 4.1: Mapping between 5-fold translation vectors and basis vectors of the 6-dimensional lattice.

Ten 3-fold translation vectors within icosahedral constellation in the quasicrystal are identified and mapped onto ten coordinates of the 6-dimensional lattice listed in Table 4.2.

5-fold translation vectors	Coordinates of the 6-dimensional lattice
$\mathbf{b}_1^1 = (1, 1, 1)$	(0.5,0.5,0.5,0.5,0.5,0.5)
$\mathbf{b}_1^2 = (1, -1, 1)$	(0.5,-0.5,0.5,0.5,-0.5,0.5)
$\mathbf{b}_1^3 = (1, 1, -1)$	(-0.5,0.5,0.5,-0.5,0.5,0.5)
$\mathbf{b}_1^4 = (1, -1, -1)$	(-0.5,-0.5,0.5,-0.5,-0.5,0.5)
$\mathbf{b}_1^5 = (0, \tau - 1, \tau)$	(0.5,-0.5,0.5,-0.5,-0.5,-0.5)
$\mathbf{b}_1^6 = (0, \tau - 1, -\tau)$	(0.5,-0.5,-0.5,-0.5,-0.5,0.5)
$\mathbf{b}_1^7 = (\tau - 1, \tau, 0)$	(0.5,0.5,-0.5,-0.5,-0.5,-0.5)
$\mathbf{b}_1^8 = (\tau - 1, -\tau, 0)$	(-0.5,0.5,-0.5,0.5,-0.5,-0.5)
$\mathbf{b}_1^9 = (\tau, 0, \tau - 1)$	(-0.5,0.5,0.5,-0.5,-0.5,-0.5)
$\mathbf{b}_1^{10} = (\tau, 0, -\tau + 1)$	(0.5,0.5,-0.5,0.5,-0.5,0.5)

Table 4.2: Mapping between 3-fold translation vectors and coordinates in the 6-dimensional lattice.

The lifting is achieved by mapping nearest-neighbor bonds ν that align with the 5-fold or 3-fold translation vectors to 6-dimensional lattice points $\mathbf{x}^{6D}$.

I can perform two orthogonal projections on the 6-dimensional coordinates obtained via lifting process using the two projection operators $\mathbf{P}^{\perp}$ and $\mathbf{P}^{\parallel}$:

$$\mathbf{P}^{\perp} = \frac{1}{\sqrt{\tau^2 + 1}} \begin{pmatrix} 0 & -1 & \tau & 0 & 1 & \tau \\ -1 & \tau & 0 & 1 & \tau & 0 \\ \tau & 0 & -1 & \tau & 0 & 1 \end{pmatrix} \tag{4.2}$$

$$\mathbf{P}^{\parallel} = \frac{1}{\sqrt{\tau^2 + 1}} \begin{pmatrix} 0 & \tau & 1 & 0 & -\tau & 1 \\ \tau & 1 & 0 & -\tau & 1 & 0 \\ 1 & 0 & \tau & 1 & 0 & -\tau \end{pmatrix} \tag{4.3}$$

The first projection using the projection operator $\mathbf{P}^{\perp}$ maps 6-dimensional lattice points into complementary (perpendicular) space $\mathbf{P}^{\perp}(\mathbf{x}^{6D}) = \mathbf{x}^{\perp}$. The second pro-

jection using the projection operator $\mathbf{P}^{\parallel}$ maps 6-dimensional lattice points to the phonon-corrected positions in physical (parallel) space $\mathbf{P}^{\parallel}(\mathbf{x}^{6D}) = \mathbf{x}^{\parallel}$.

4.4.7 Phason Strain Analysis

Details of the phason strain analysis are provided in the supplementary information of literature (R1). I analyze the long-range order in a structure (a rational approximant or an IQC with structural defects) and compare it with the expectations from the theory of quasicrystal. For the particle positions lifted onto the 6-dimensional lattice $\mathbf{x}_p^{6D}$, where p is a particle index, the relationship of the distance between phonon-corrected particle positions in physical space, $r_{i,j}^{\parallel} = \left|\mathbf{P}^{\parallel}(\mathbf{x}_i^{6D}) - \mathbf{P}^{\parallel}(\mathbf{x}_j^{6D})\right| = \left|\mathbf{x}_i^{\parallel} - \mathbf{x}_j^{\parallel}\right|$, and the corresponding distance in complementary space, $r_{i,j}^{\perp} = \left|\mathbf{P}^{\perp}(\mathbf{x}_i^{6D}) - \mathbf{P}^{\perp}(\mathbf{x}_j^{6D})\right| = \left|\mathbf{x}_i^{\perp} - \mathbf{x}_j^{\perp}\right|$, characterizes the phason displacement. I determine the average distance of two particles in complementary space as a function of their distance in physical space:

$$r^{\perp}(r^{\perp}) = \left\langle r_{i,j}^{\perp} \middle| r_{i,j}^{\parallel} \right\rangle_{i,j} \simeq \left\langle r_{i,j}^{\perp} \middle| r_{i,j}^{\parallel} \leq r_{i,j}^{\parallel} \leq r_{i,j}^{\parallel} + \Delta r \right\rangle_{i,j} \tag{4.4}$$

The angle brackets denote an average over particles pairs that have a distance in physical space within the interval $[r_{i,j}^{\parallel}, r_{i,j}^{\parallel} + \Delta r]$. Because of the discreteness of the 6-dimensional lattice, I need to use a small but finite interval of width Δr. In the limit of large $r_{\parallel}$, the cut and project theory [28] predicts a linear behavior:

$$\lim_{r^{\parallel} \to \infty} r^{\perp}(r^{\perp}) = \alpha r^{\parallel} + \beta \tag{4.5}$$

Here, α is a measure for the phason strain and β is a measure for the size of the acceptance window.

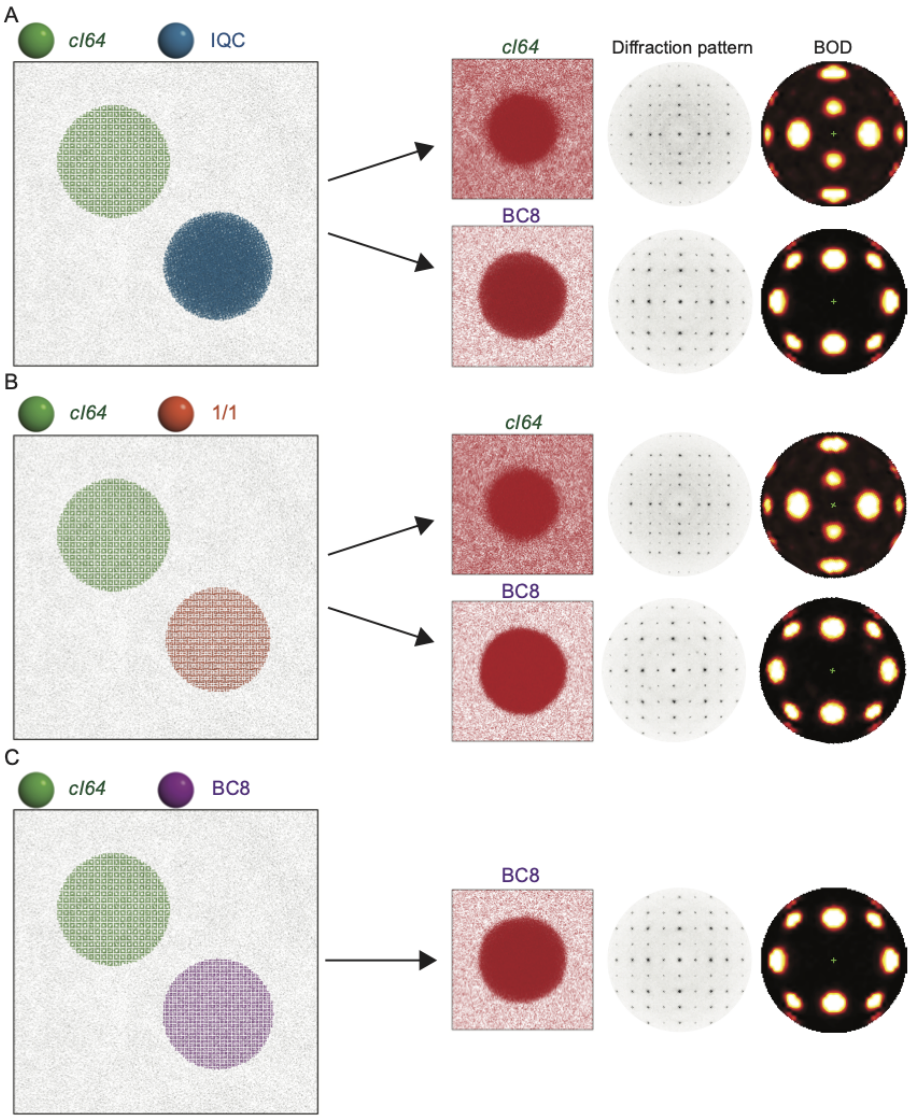

Figure 4.4: Simulations of competition of crystal growth between competing phases (A-C) (left) A snapshot of the initial configuration of the simulation, where two competing phases are placed within a gas of 96,000 particles; a $cI64$ (green, $N = 24{,}000$) and an IQC (blue, $N = 24{,}000$) (A), a $cI64$ (green, $N = 24{,}000$) and a relaxed approximant with phason strain 0.08154 (approximant constructed with a slope 1/1) (orange, $N = 24{,}000$) (B), a $cI64$ (green, $N = 24{,}000$) and a $BC8$ (purple, $N = 24{,}000$) (C). Number density and temperature of system are kept constant as $N/V = 0.092$ and $k_BT/\epsilon = 0.25$ for all simulations. The two phases compete freely during a simulation, and (right) at the end of simulation, I identify the final phase using direct visualization, diffraction pattern, and BOD. For all the simulations, I observe formation of $BC8$ crystals. For (A) and (B), I sometimes observe growth of the $cI64$. These results indicate that cI64 is a metastable phase that is more stable than IQC or the approximant. $BC8$ is the most stable phase among the competing phases.

CHAPTER V

Flexible Crystallization of Colloidal Polyhedra by Design

This chapter is adapted from a publication in preparation, authored by Wenjie Zhou, Yuanwei Li, Kwanghwi Je, Thi Vo, Haixin Lin, Benjamin E. Partridge, Ziyin Huang, Sharon C. Glotzer, and Chad A. Mirkin. This is a collaborative work with the Mirkin's group at the Northwestern University. My collaborators performed all experimental work. My major contribution to this work is designing simplified simulation model for polyhedron nanocrystals and performing Molecular Dynamics simulations of the model particles. Thi Vo performed theoretical calculations.

5.1 Introduction

Superlattices composed of nanocrystals displays considerable promise for the development of nanostructures with vibrational and optical properties [7, 66, 67]. To fully explore these properties that depend on nanocrystal arrangements, it is highly desirable to control crystal symmetries and domain size of superlattices. Self-assembly of polyhedral nanocrystal (pNC) offer a compelling platform to synthesize superlattices with control over size and crystal symmetry [9]. Indeed, self-assembly approaches based on sedimentation or evaporation have realized large pNC superlattices with various crystal symmetries [68, 69]. However, superlattices prepared from those approaches are by and large limited to a few close packed structures, which

limits their versatility in applications.

Coating DNA ligands on pNCs can provide an additional powerful handle for assembling superlattices with wider ranges of crystal symmetries [70, 71, 72, 73, 10]. Through the interplay between pNC shape and ligand shell, DNA mediated self-assembly can even direct formation of pNC superlattices with complex symmetry [74, 75], including clathrate crystals [11]. However, it remains challenging to employ DNA-mediated pNC assembly for accessing superlattices with certain symmetries. The bulky nature of DNA ligands can alter the native geometries of the original polyhedral shape [75], which can prevent assembly of pNC arrangements arising solely from particle shape. For example, DNA functionalization of octahedral NCs usually drive particle organization into body-centered-cubic (*bcc*) crystals [72], in direct contrast to the assembly of *Minkowski* or monoclinic crystals arising solely from particle shape of octahedral NCs [68]. In an attempt to decouple the contributions between ligand shell and core shape in driving pNCs assembly, shorter DNA lengths have been employed, yet unable to produce highly ordered crystals [11, 72, 76]. Such lack of ordering likely arises due to a) limited flexibility of the short DNA strands, which is unable to compensate for the intrinsic polydispersity of pNCs; and b) the high charge densities induced by DNA. Another challenge yet to be met in DNA-mediated assembly is producing pNC superlattices with large domain size. Majorities of DNA-mediated assembly approaches could only produce pNC superlattices with domain size up to 5 micrometers [72, 73, 76], which could limit functionality stemming from long-range nanocrystal arrangements. Therefore, to utilize DNA as a tool for creating pNC assemblies with desired functions, it is essential to design ligands that reliably produce large superlattices and promise access to various pNC arrangements with different crystal symmetries.

Previous studies on NC assemblies shed light on the role of the flexible ligand shell in a formation of superlattices with unusual crystal symmetries [75]. In DNA-mediated nanosphere-assemblies, recent works have shown that incorporating flexible region into DNA ligands can increase the domain size of superlattices or drive transitions in crystal structures [77, 78, 79]. Building on these ideas of using flexible ligands, my collaborators present a new DNA design featuring a flexible, charge-neutral region adjacent to the sticky end that facilitates the assembly of various pNCs into superlattices with large domain and a broad range of lattice symmetries. The flexible DNA design can minimally alter the native geometries of pNCs and guide assembly of some superlattices arising solely from particle shape. By considering the spatial distribution of DNA ligands on particle surface, I show that the assembly of DNA-coated octahedra into a specific superlattice can be predicted by molecular simulations. The DNA design proposed in this work greatly expands the diversity in pNC arrangements and would pave the way to devise large nanostructures with functionalities.

5.2 Results

5.2.1 Assembly Behavior of DNA-coated Polyhedron in Experiments

Oligoethylene glycol (OEG) spacers are a type of highly flexible, charge neutral chemical modification that can be incorporated into synthetic oligonucleotides, and thus collaborators utilized these moieties as the flexible region in their new DNA design. DNA strands featuring n hexaethyleneglycol units (spn, n = 0, 1, 2, 3, 5) were designed with self-complementary sticky ends that can hybridize to the sticky ends on any other particle in the system. With the DNA design, collaborators observed that increasing the number of OEG spacer can facilitate assembly of superlattices with large crystal domain. In the assemblies of DNA-coated octahedra, collaborators

found that crystal symmteries of superlattices depended on the ratio of octahedron edge length to DNA ligand length; as the ratio decreases, structural transitions occur from a simple hexagonal crystal (sh) to a $Minkowski$ crystal and then a high-pressure lithium crystal with space-group I-43d ($I-43d$), followed by a transition to a body-centered-cubic (bcc) crystal. Using this design, collaborators also observed co-crystallization of three space-filling polyhedron mixtures and one non-space-filling polyhedron mixture. In particular, the non-space-filling mixture, binary mixture of decahedra and octahedra, assembled into complex superlattices with local structures that can be mapped to the patterns found in Penrose $P1$ tiling. In the following, I will refer to this complex superlattice as a $P1$ superlattice.

5.2.2 Accessing Diverse Structures in DNA-mediated Assemblies of Octahedra

The observed phase behaviors of octahedron self-assembly can be qualitative explained by characterizing the DNA spatial distribution about the core octahedron [75, 80]. Given the same ligand length, as core size decreases, DNA preferentially partition towards the edges and corners of the octahedron (Fig.5.3). This is a result of two cooperative effects. Firstly, ligands experience a net increase in confinement energy as a result of being anchored to an increasingly smaller area. Secondly, the same ligand appears effectively bigger to a smaller core relative to a larger core. This enunciates the entropic gain afforded by higher curvature locations on the core surface, creating a stronger partitioning driving force. Physically this means that larger octahedra have higher DNA ligand concentrations on their faces, which favors close-packed face-face alignments and thus the sh phase. Smaller octahedra conversely have a higher ligands concentration at the corners and edges, favoring corner/edge alignments that result in open lattices like bcc phase.

Considering the spatial distribution of DNA ligands, Thi Vo predicted the phase

behavior of octahedron. Thi Vo used thermodynamic perturbation theory (TPT) [81] in conjunction with the spatial distribution of DNA-graft to compute lattice free energy of formation of competing structure. Lattice energies were calculated across a range of octahedron edge length E from 20 nm to 120 nm, and the length of DNA ligand L was kept constant at 10 nm. For a wide range of edge lengths, there is a nice agreement between experimental assembly behavior and theoretical predictions.

To verify morphology predicted by TPT, I performed molecular dynamics (MD) simulations of simplified pNC model using Hoomd-Blue simulation toolkit.[24, 63, 26] In this simple model, a single pNC was represented as a rigid polyhedron core surrounded by a DNA ligand shell. The interaction between flexible DNA ligand was modeled by effective potentials (see section 5.4.2). To account for the spatial distribution of DNA-graft, interaction of DNA ligands on facets got stronger as the edge length to ligand length ratio (E/L) increased. I selected four relative edge length to ligand length ratios (E/L) = [12, 7, 6, and 3] and simulated the crystallization of model pNCs. I then characterized the morphology of octahedron assemblies by diffraction patterns. For (E/L) = 12, 7, 6, and 3, I observed the formation of sh (Fig.5.1A, E), $Minkowski$ (Fig.5.1B, F), $I-43d$ (Fig.5.1C, G), and bcc (Fig.5.1D, H), which match with experiments. My MD simulations emphasize that spatial distribution of flexible DNA ligands plays a crucial role in pNC crystallization behavior, which is consistent with previous reports [75].

5.2.3 Molecular Dynamics Simulations of Co-crystallization

Using MD simulations of model polyhedra, I further reproduced the experimental assembly of 3 space-filling polyhedron pairs. By simulating crystal formation from disordered fluid, I observed spontaneous formation of a $CsCl$ crystal from the mixture of octahedron and cuboctahedron with a 1:1 stoichiometric composition, a tetra-octa

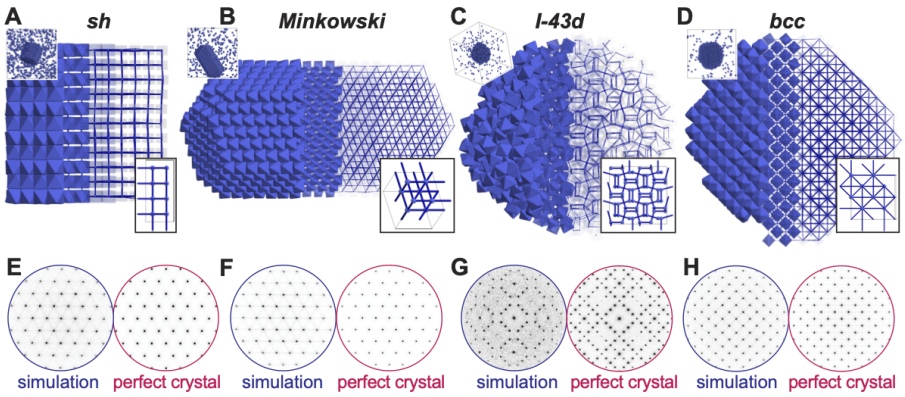

Figure 5.1: Assembly of a diverse set of pNC superlattices. (A-D) Schematics of *sh* (A), *Minkowski* (B), $I-43d$ (C), and *bcc* (D) superlattices of octahedra. (E-H) SEM images of superlattices of octahedral NCs corresponding to (A-D). (I) Experimental phase diagram for octahedron-assembled superlattices as a function of edge length E and DNA length L. At $L = 10$ nm, the experimental phase diagram is overlaid by color-coded boxes representing theoretical phase diagram. (J) Lattice energies of competing structures near the regime $(E/L) \simeq 8$. (A-D) Superlattices of octahedra assembled in molecular dynamics (MD) simulations. In each figure, a snapshot of simulation box (top left), solid clusters extracted from the snapshot (center), and 2×2×2 unit cells of crystals (bottom right) are shown. With decreasing E/L, octahedra assemble into *sh* (A), *Minkowski* (B), $I-43d$ (C), and *bcc* (D) phases. For solid clusters, the transparency of octahedron is increased from left to right to show local coordination. (E-H) Diffraction patterns obtained from snapshots in (A-D) (left) and from perfect crystals (right), showing the same symmetry and peak positions.

honeycomb (*toh*) crystal from the mixture of octahedron and tetrahedron with a 1:2 stoichiometric composition, and a gyrated tetra-octa honeycomb (*gtoh*) crystal from the mixture of octahedron and bitetrahedron with a 1:1 stoichiometric composition (Fig.5.2A-C). The diffraction patterns of the self-assembled superlattices show well-defined Bragg peaks that correspond to $CsCl$, *toh*, and *gtoh* phases. I note that these crystal phases can be assembled from binary mixtures of hard polyhedra, which suggests that shape complementarity between these space-filling polyhedron pair is the essential feature driving the self-assembly of these superlattices and that the proposed flexible DNA ligands can minimally alter the shape complementarity.

The DNA-mediated assembly of $P1$ superlattices from a non-space-filling pair was also confirmed by MD simulations. I simulated assembly of binary mixtures of

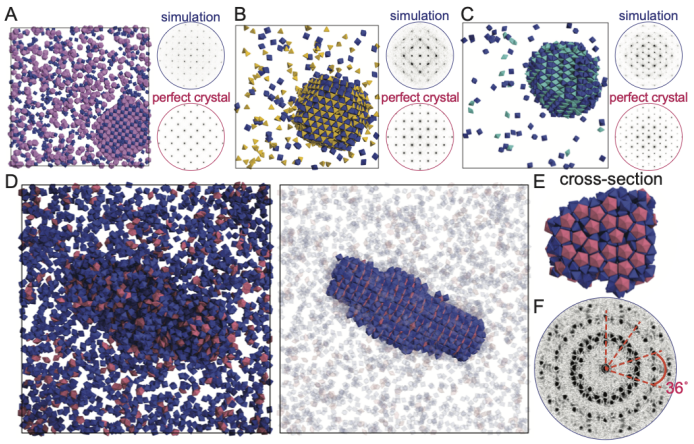

Figure 5.2: MD simulations of co-crystallization. (A-C) Assembly of $CsCl$ phase from DNA-coated cuboctahedra (purple) and octahedra (blue) (A), *toh* phase from DNA-coated tetrahedra (yellow) and octahedra (blue) (B) and *gtoh* phase from DNA-coated bitetrahedra (cyan) and octahedra (blue) (C). Left panels show MD simulation snapshots of the particle assemblies. Right panels show diffraction patterns obtained from the snapshots (upper right) and from perfect crystals (lower right). Diffraction patterns show the same symmetry and peak positions. (D) Snapshots obtained from MD simulations of binary mixture of DNA-coated decahedra (red) and octahedra (blue). The same snapshot is shown twice: (left) the particle assembly and (right) to visualize the $P1$ superlattice in the assembly, particles not belonging to the superlattice are colored translucently. The superlattice is a periodic stacking of layers. (E) Cross-section of the $P1$ superlattice viewed along the stacking direction. (F) Diffraction patterns of the $P1$ superlattice, indicating decagonal symmetry.

decahedron and octahedron with 1:4 stoichiometric composition and observed formation of a $P1$ superlattice that consisted of a periodic stacking of layers (Fig.5.2D). Cross-section of the $P1$ superlattice viewed along the stacking direction (Fig.5.2E) shows local structures that can be mapped to the patterns found in Penrose $P1$ tiling. The diffraction patterns of $P1$ superlattices viewed along the stacking direction showed a decagonal symmetry (Fig.5.2F). I note that binary mixtures of hard decahedron and hard octahedron did not assemble into $P1$ superlattices but assembled into periodically ordered crystals with two-fold and six-fold rotational symmetries. This result demonstrates that the flexible DNA-graft can alter the crystallization behavior of the non-space-filling pair, decahedron and octahedron, unlike other space-tilling polyhedron pairs. Taken together, the assembly of octahedron and

that of decahedron-octahedron mixtures illustrate that I can employ flexible DNA-grafts as an additional design handle for tuning the arrangements of non-space-filling polyhedra.

5.3 Discussion

The ability to engineer new structures by design using geometric considerations and DNA-mediated interactions unleashes an immense opportunity to explore an enormous library of new structures, of which the 10 presented here represent a small fraction. Considering the recent interest in highly ordered plasmonic superlattices in the field of optical metamaterials, the presented DNA- assembly approach would be particularly advantageous for realizing materials with novel functionalities and exploring structure-function relationships. More broadly, a fundamental understanding of geometry-induced organization is easily translatable to other systems of anisotropic particles beyond gold pNCs. As a result, the design outlined in this work would provide insights into spontaneous organization of materials from a spectacular variety of building blocks of different shapes.

5.4 Methods and Supporting Information

5.4.1 Molecular Dynamics Simulation

Molecular dynamics (MD) simulations with the anisotropic Weeks–Chandler–Anderson (aWCA) framework [26] are performed to simulate the assembly behavior of DNA-coated polyhedral nanocrystals. The aWCA framework is implemented in the Hoomd-Blue simulation package [24]. Most MD simulations of the present work were run on a NVIDA Tesla V100 graphics processing unit (GPU) at XSEDE [63]. I perform MD simulations with between N = 2,000 and N = 20,000 model polyhedral nanocrystals, which is large enough to form a sufficient number of superlattice unit cell. I use

periodic boundary conditions and simulate for at least 6×10 time steps in individual runs. All simulations are performed in the NVT ensemble at particle volume fraction $\phi = N\nu_0/V = 0.05$, where N is the number of polyhedral nanocrystals, ν_0 is the volume of polyhedron, and V is the volume of simulation box. MD simulation results are discussed in Simulations and Theoretical Predictions sections 5.4.3. - 5.4.4

5.4.2 Minimal Model for DNA-coated Polyhedral Nanocrystals

I constructed a coarse-grained simulation model in which a single polyhedral nanocrystal is represented as a polyhedron core surrounded by a DNA ligand shell (Fig.5.4). This model assumes four structural features of DNA-functionalized polyhedral nanocrystals: (i) the double-stranded DNA (ds-DNA) shell is non-attractive; (ii) the DNA shell causes an effective rounding of the polyhedral core; (iii) the oligonucleotides and single-stranded DNA region are flexible and attractive; (iv) as the ratio of edge length (E) to the ligand length (L) increases, interactions of ligands near facets become relatively stronger than those between vertices [72, 75].

The polyhedron core and DNA shell are modeled using the aWCA framework, where rounded polyhedron cores interact with each other via a pairwise potential V_{WCA} that combines the isotropic Weeks–Chandler–Anderson potential $V_{WCA,0}$ and contact Weeks–Chandler–Anderson potential $V_{WCA,c}$.

$$V_{WCA}(r) = V_{WCA,0}(r) + V_{WCA,c}(r) \tag{5.1}$$

$$V_{WCA,0}(r) = 4\epsilon_{WCA,0}\left[(\frac{\sigma_{WCA,0}}{r})^{12} - (\frac{\sigma_{WCA,0}}{r})^{6}\right] \tag{5.2}$$

$$V_{WCA,c}(r) = 4\epsilon_{WCA,c}\left[(\frac{\sigma_{WCA,c}}{r})^{12} - (\frac{\sigma_{WCA,c}}{r})^{6}\right] \tag{5.3}$$

$V_{WCA,0}(r)$ is repulsive isotropic interaction that depends on radial distance r between polyhedron center of masses. $V_{WCA,c}(r)$ is repulsive contact interaction be-

tween closest facet pair and depends on contact distance r_c, which is the function of the radial distance r and polyhedron orientations. $\sigma_{WCA,0}$ is the insphere diameter of polyhedron core and $\sigma_{WCA,c}$ is a parameter that determines the effective rounding of polyhedron core. Here, I set the rounding radius $\sigma_{WCA,c}/2$ to be the length of DNA ligands, which is parameterized from the ligand length (L) used in experiments. $\epsilon_{WCA,c}$ is the energy for contact interaction and $\epsilon_{WCA,0}$ is the energy for isotropic interaction that depends on $\epsilon_{WCA,c}$, radial distance r, $\sigma_{WCA,0}$, $\sigma_{WCA,c}$ and polyhedron orientations [26]. The cutoff distances for $V_{WCA,0}$ and $V_{WCA,c}(r)$ are $r = \sigma_{WCA,0} \times 2^{1/6}$ and $r_c = \sigma_{WCA,c} \times 2^{1/6}$, respectively. I shift the potential at the cutoff distances.

Oligonucleotides and single-strand DNA are modeled by patches that are precisely located inside the polyhedral nanocrystals. Here, I consider vertex type patch and facet type patch that interact via a shifted-gaussian potential V_{sg}.

$$V_{sg}(r) = \epsilon_{sg} exp\left[-\frac{1}{2}(\frac{r - r_0}{\sigma_{sg}})\right] \tag{5.4}$$

r is the distance between patch centers and r_0 denotes the distance, where DNA hybridization occurs. σ_{sg} is a width of attractive well that determines flexibility of attractive patch-patch interaction. ϵ_{sg} is the energy for patch interaction. Vertex and facet patches are located on vertex and facet of small polyhedron, which is obtained by uniform scaling of polyhedron core by a scale factor less than 1. Here, vertex and facet patch represent attractive interaction near vertex and facet respectively. As the ratio of edge length (E) to the ligand length ($L \simeq \sigma_{WCA,c}/2$) increases, I increased ϵ_{sg} of interaction between facet patches while fixing the ϵ_{sg} of interaction between vertex patches. This reflects the geometric feature (iv) where shorter ligands result in face-face interaction stronger than vertex-vertex interaction. I cut the potential at $r = r_{sg,cut}$. The geometry of polyhedron core, spatial coordinates of the patch positions,

and the values of potential parameters are listed in Supplementary Tables 5.1-5.13. I note that my model may not capture all the details of atomistic interactions between DNA ligands. I motivate simple model through its qualitative and quantitative resemblance to experimental results.

5.4.3 Molecular Dynamics Simulation Results: octahedron

I studied the assembly behavior of octahedra with different ratios of edge length (E) to ligand length (L); I kept the edge length E constant and changed the value of L, which is set to be $\sigma_{WCA,c}/2$ (Methods and supporting information section 5.4.2). For octahedron with $E/L \simeq 3$ and $E/L \simeq 6$, I initialized a disordered cluster of N = 2,000 octahedra and annealed the cluster at constant temperature for sufficient time until crystallization was observed. Octahedra with $E/L \simeq 3$ and $E/L \simeq 6$ self-assembled into *bcc* crystal and $I-43dcrystal$, respectively (figs. S22, S23). The results of self-assembly simulations are in good agreement with experimental assembly behavior.

For $E/L \simeq 12$, I did not observe self-assembly of *sh* phase. However, I found that sh phase could grow from a seed of 128 octahedra and that sh phase was stable than competing structures, which were *bcm*, $Minkowski$, and $I-43d$. These results demonstrate that sh phase is stable with the selected octahedron model in my simulations, which match with theoretical predictions and experimental assembly behavior.

For $E/L \simeq 7$, I observed that $Minkowski$ phase could grow from a seed of 128 octahedra and that observed $Minkowski$ phase is stable than competing structures, which were *sh*, $I-43d$, and *bcm*. These results demonstrate that $Minkowski$ phase is stable with the selected octahedron model in my simulations, which match with theoretical predictions.

5.4.4 Molecular Dynamics Simulation Results: Binary Mixtures of pNCs

For the self-assembly simulation of the binary mixture of octahedron and tetrahedra, I initialized a disordered cluster of $N = 667$ octahedra and $N = 1{,}333$ tetrahedra and annealed the cluster at constant temperature $k_BT = 1.83$ $(unit\ \epsilon)$. Upon annealing, I observed self-assembly of *toh* crystal.

For the self-assembly simulation of the binary mixture of octahedron and bitetrahedron, I initialized a disordered cluster of $N = 1{,}000$ octahedra and $N = 1{,}000$ bitetrahedra and annealed at constant temperature $k_BT = 1.71$ $(unit\ \epsilon)$. I observed self-assembly of *gtoh* crystal upon annealing.

For the binary mixture of octahedron and cuboctahedron, I observed self-assembly of $CsCl$ crystal upon annealing a disordered cluster of $N = 1{,}000$ octahedra and $N = 1{,}000$ cuboctahedra at constant temperature $k_BT = 1.50$ $(unit\ \epsilon)$. I sometimes observe that the binary mixtures phase separate into *sc* lattice of cuboctahedra and $I - 43d$ lattice of octahedra. Possible reasons for the phase separation can be that the mixture of the two phases is competing with $CsCl$ phase or that my simple models may not fully capture all the features of interparticle interactions for $CsCl$ assemblies. I leave a more detailed discussion of the $CsCl$ assemblies to future work.

For the self-assembly simulation of the binary mixture of octahedron and tetrahedron, I initialized a disordered cluster of $N = 4{,}000$ octahedra and $N = 1{,}000$ decahedra and annealed at constant temperature $k_BT = 3.34$ $(unit\ \epsilon)$. I observed self-assembly of a $P1$ superlattice upon annealing. To obtain a large single domain of a $P1$ superlattice, I conducted a seed-assisted growth simulation. In a thin simulation box, I placed a seed of $N = 880$ octahedra and $N = 288$ decahedra within a fluid of 15,120 octahedra and 3712 decahedra. Here, the seed was excised from a large superlattice grown from the self-assembled superlattice shown in Fig. 5D. The seed

was placed with the 10-fold axis of the seed pointed along the thin box dimension. Upon annealing at constant temperature $k_BT = 3.34$ ($unit\ \epsilon$), a $P1$ superlattice grew in the quasiperiodic plane perpendicular to the short box axis. The grown superlattice exhibit 10-fold symmetry and can be mapped to a pattern resembling Penrose $P1$ tiling.

5.4.5 Hard Particle Monte Carlo Simulations

To compare assembly behavior of DNA-coated polyhedron mixture and hard polyhedron mixture, I perform hard particle Monte Carlo (HPMC) simulations [23] of hard polyhedron mixtures. I conducted the HPMC simulation on multiple central processing units (CPUs) with message passing interface domain decomposition. All simulations were performed in the isochoric ensemble with periodic boundary conditions. For each simulation, I initialized system by placing particles randomly at very low volume fraction $\phi = 0.008$ and then rapidly compressed simulation box until the target volume fraction was reached. After compression, I equilibrated the compressed system until crystallization was observed. Typically, crystallization occurred within 10^8 Monte Carlo sweeps. I identified the crystal phases based on the diffraction patterns. I observed that binary mixture of 3,658 cuboctahedra and 7,316 octahedra self-assemble to $CsCl$ crystals at volume fraction $\phi = 0.57$. Binary mixture of 7,316 tetrahedra and 3,658 octahedra self-assemble to *toh* crystals at volume fraction $\phi = 0.515$. Binary mixture of 5,488 bitetrahedra and 5,488 octahedra self-assemble to *gtoh* crystals at volume fraction $\phi = 0.55$. Binary mixture of 2,195 decahedra and 8,780 octahedra self-assemble to hexagonal crystals at volume fraction $\phi = 0.57$.

5.4.6 Phase Identification from Simulation Results

I identified the crystal phases based on visual inspection and diffraction patterns. Diffraction patterns are obtained by projecting the centers of particles into a plane along high-symmetry axes and then applying a fast Fourier transform. For complex $P1$ superlattice, I used a combination of Steinhardt order parameters [64, 82] to distinguish particles that are part of the $P1$ superlattice from those that belong to the fluid. I created the set of vectors connecting the center of a decahedron to the centers of the 10 closest octahedra, and computed the Steinhardt order parameters q_2, q_3, and q_4 from the vector set. If order parameters satisfy $q_2 < 0.15$, $q_3 < 0.20$, and $0.30 < q_4 < 0.45$ conditions, particles are identified as solid.

5.4.7 Geometry of Polyhedron, Spatial Coordinates of Patch Positions, and Values of Potential Parameters

Octahedron							
Vertex positions of polyhedron core							
	x	y	z		x	y	z
1	2.0	0.0	0.0	2	-2.0	0.0	0.0
3	0.0	2.0	0.0	4	0.0	-2.0	0.0
5	0.0	0.0	2.0	6	0.0	0.0	-2.0
Patch positions in the polyhedron core							
Vertex patch				Facet patch			
1	1.0	0.0	0.0	1	0.33333	0.33333	0.33333
2	-1.0	0.0	0.0	2	-0.33333	0.33333	0.33333
3	0.0	1.0	0.0	3	0.33333	-0.33333	0.33333
4	0.0	-1.0	0.0	4	0.33333	0.33333	-0.33333
5	0.0	0.0	1.0	5	-0.33333	-0.33333	-0.33333
6	0.0	0.0	-1.0	6	0.33333	-0.33333	-0.33333
				7	-0.33333	0.33333	-0.33333
				8	-0.33333	-0.33333	0.33333

Table 5.1: Coordinates of octahedron core vertices and patch positions used for simulations.

Tetrahedron							
Vertex positions of polyhedron core							
	x	y	z		x	y	z
1	1.0	1.0	1.0	2	1.0	-1.0	-1.0
3	-1.0	1.0	-1.0	4	-1.0	-1.0	1.0
Patch positions in the polyhedron core							
Vertex patch				Facet patch			
1	0.43	0.43	0.43	1	0.14333	0.14333	-0.14333
2	0.43	-0.43	-0.43	2	-0.14333	0.14333	0.14333
3	-0.43	0.43	-0.43	3	0.14333	-0.14333	0.14333
4	-0.43	-0.43	0.43	4	-0.14333	-0.14333	-0.14333

Table 5.2: Coordinates of tetrahedron core vertices and patch positions used for simulations.

Bitetrahedron							
Vertex positions of polyhedron core							
	x	y	z		x	y	z
1	0.0	1.63300	0.0	2	0.0	-0.81650	-1.41421
3	0.0	-0.81650	1.41421	4	-2.30940	0.0	0.0
5	2.30940	0.0	0.0				
Patch positions in the polyhedron core							
Vertex patch				Facet patch			
1	0.0	0.92591	0.0	1	-0.43648	0.15432	-0.26729
2	0.0	-0.46295	-0.80186	2	-0.43648	0.15432	0.26729
3	0.0	-0.46295	0.80186	3	-0.43648	-0.30864	0.0
4	-1.30943	0.0	0.0	4	0.43648	0.15432	-0.26729
5	1.30943	0.0	0.0	5	0.43648	0.15432	0.26729
				6	0.43648	-0.30864	0.0

Table 5.3: Coordinates of bitetrahedron core vertices and patch positions used for simulations.

Cuboctahedron							
Vertex positions of polyhedron core							
	x	y	z		x	y	z
1	2.0	2.0	0.0	2.0	2.0	-2.0	0.0
3	2.0	0.0	2.0	4	2.0	0.0	-2.0
5	-2.0	2.0	0.0	6	-2.0	-2.0	0.0
7	-2.0	0.0	2.0	8	-2.0	0.0	-2.0
9	0.0	2.0	2.0	10	0.0	2.0	-2.0
11	0.0	-2.0	2.0	12	0.0	-2.0	-2.0
Patch positions in the polyhedron core							
Vertex patch				Facet patch (Triangle facet)			
1	1.292	1.292	0.0	1	0.86133	-0.86133	-0.86133
2	1.292	-1.292	0.0	2	0.86133	-0.86133	0.86133
3	1.292	0.0	1.292	3	0.86133	0.86133	-0.86133
4	1.292	0.0	-1.292	4	0.86133	0.86133	0.86133
5	-1.292	1.292	0.0	5	-0.86133	-0.86133	-0.86133
6	-1.292	-1.292	0.0	6	-0.86133	-0.86133	0.86133
7	-1.292	0.0	1.292	7	-0.86133	0.86133	-0.86133
8	-1.292	0.0	-1.292	8	-0.86133	0.86133	0.86133
9	0.0	1.292	1.292				
10	0.0	1.292	-1.292				
11	0.0	-1.292	1.292				
12	0.0	-1.292	-1.292				
Facet patch (Square facet)							
1	0.646	0.0	-1.292	2	-1.292	0.646	0.0
3	-0.646	0.0	-1.292	4	-1.292	-0.646	0.0
5	0.0	0.646	-1.292	6	-1.292	0.0	0.646
7	0.0	-0.646	-1.292	8	-1.292	0.0	-0.646
9	0.646	0.0	1.292	10	0.646	-1.292	0.0
11	-0.646	0.0	1.292	12	-0.646	-1.292	0.0
13	0.0	0.646	1.292	14	0.0	-1.292	0.646
15	0.0	-0.646	1.292	16	0.0	-1.292	-0.646
17	1.292	0.646	0.0	18	0.646	1.292	0.0
19	1.292	-0.646	0.0	20	-0.646	1.292	0.0
21	1.292	0.0	0.646	22	0.0	1.292	0.646
23	1.292	0.0	-0.646	24	0.0	1.292	-0.646
Note: I set facet patches for triangle facet and square facet of cuboctahedron separately. In this way, I can model the interactions of DNA ligands on triangle facet and square facet separately.							

Table 5.4: Coordinates of cuboctahedron core vertices and patch positions used for simulations.

Decahedron							
Vertex positions of polyhedron core							
	x	y	z		x	y	z
1	0.0	2.40600	0.0	2	-2.28827	0.74349	0.0
3	-1.41422	-1.94650	0.0	4	1.41422	-1.94650	0.0
5	2.28827	0.74349	0.0	6	0.0	0.0	-1.48699
7	0.0	0.0	1.48699				
Patch positions in the polyhedron core							
Vertex patch				Facet patch			
1	0.0	1.40511	0.0	1	-0.44545	0.61310	-0.28947
2	-1.33635	0.43420	0.0	2	-0.44545	0.61310	0.28947
3	-0.82590	-1.13675	0.0	3	-0.72075	-0.23418	-0.28947
4	0.82590	-1.13675	0.0	4	-0.72075	-0.23418	0.28947
5	1.33635	0.43420	0.0	5	0.0	-0.75784	-0.28947
6	0.0	0.0	0.86840	6	0.0	-0.75784	0.28947
7	0.0	0.0	-0.86840	7	0.72075	-0.23418	-0.28947
				8	0.72075	-0.23418	0.28947
				9	0.44545	0.61310	-0.28947
				10	0.44545	0.61310	0.28947

Table 5.5: Coordinates of Decahedron core vertices and patch positions used for simulations.

Octahedron ($E/L \simeq 2E/\sigma_{WCA,c} \simeq 12$)					
Timestep		dt = 0.0003			
Parameters for potential					
aWCA					
	$\epsilon_{WCA,c}$	$\sigma_{WCA,0}$	$r_{WCA,0cut}$	$\sigma_{WCA,c}$	$r_{WCA,ccut}$
Octahedron - Octahedron	1.0	2.3094 - 2.3094	2.5922	0.4711	0.5288
shifted-gaussian					
		ϵ_{sg}	σ_{sg}	r_0	$r_{sg,cut}$
Octahedron - Octahedron	vertex-vertex	1.0	0.35	2.5288	2.6152
	facet-facet	11.0	0.35	1.6835	2.5288
	vertex-facet	2.0	0.35	2.1062	2.5288

Table 5.6: Parameters for simulations of octahedron with $E/L \simeq 12$.

Octahedron ($E/L \simeq 2E/\sigma_{WCA,c} \simeq 7$)					
Timestep		dt = 0.0005			
Parameters for potential					
aWCA					
	$\epsilon_{WCA,c}$	$\sigma_{WCA,0}$	$r_{WCA,0cut}$	$\sigma_{WCA,c}$	$r_{WCA,ccut}$
Octahedron - Octahedron	1.0	2.3094 - 2.3094	2.5922	0.8037	0.9021
shifted-gaussian					
		ϵ_{sg}	σ_{sg}	r_0	$r_{sg,cut}$
Octahedron - Octahedron	vertex-vertex	1.0	0.35	2.9021	3.1676
	facet-facet	0.45	0.35	2.0568	3.1676
	vertex-facet	0.725	0.35	2.4794	3.1676

Table 5.7: Parameters for simulations of octahedron with $E/L \simeq 7$.

Octahedron ($E/L \simeq 2E/\sigma_{WCA,c} \simeq 6$)					
Timestep		dt = 0.0005			
Parameters for potential					
aWCA					
	$\epsilon_{WCA,c}$	$\sigma_{WCA,0}$	$r_{WCA,0cut}$	$\sigma_{WCA,c}$	$r_{WCA,ccut}$
Octahedron - Octahedron	1.0	2.3094 - 2.3094	2.5922	0.9329	1.0471
shifted-gaussian					
		ϵ_{sg}	σ_{sg}	r_0	$r_{sg,cut}$
Octahedron - Octahedron	vertex-vertex	1.0	0.35	3.0473	3.3217
	facet-facet	0.30	0.35	2.2020	3.3217
	vertex-facet	0.65	0.35	2.6246	3.3217

Table 5.8: Parameters for simulations of octahedron with $E/L \simeq 6$.

Octahedron ($E/L \simeq 2E/\sigma_{WCA,c} \simeq 3$)					
Timestep		dt = 0.0005			
Parameters for potential					
aWCA					
	$\epsilon_{WCA,c}$	$\sigma_{WCA,0}$	$r_{WCA,0cut}$	$\sigma_{WCA,c}$	$r_{WCA,ccut}$
Octahedron - Octahedron	1.0	2.3094 - 2.3094	2.5922	1.8868	2.1178
shifted-gaussian					
		ϵ_{sg}	σ_{sg}	r_0	$r_{sg,cut}$
Octahedron - Octahedron	vertex-vertex	1.0	0.35	4.1178	4.4135
	facet-facet	0.01	0.35	3.2725	4.4135
	vertex-facet	0.08	0.35	3.6952	4.4135

Table 5.9: Parameters for simulations of octahedron with $E/L \simeq 3$.

Binary mixture of octahedron and tetrahedron					
Timestep			dt = 0.0005		
Parameters for potential					
aWCA					
	$\epsilon_{WCA,c}$	$\sigma_{WCA,0}$	$r_{WCA,0cut}$	$\sigma_{WCA,c}$	$r_{WCA,ccut}$
Octahedron - Octahedron	1.0	2.3094 - 2.3094	2.5922	0.7726	0.8673
Octahedron - Tetrahedron	1.0	2.3094 - 1.1547	1.9442	0.7726	0.8673
Tetrahedron - Tetrahedron	1.0	1.1547 - 1.1547	1.2961	0.7726	0.8673
shifted-gaussian					
		ϵ_{sg}	σ_{sg}	r_0	$r_{sg,cut}$
Octahedron - Octahedron	vertex-vertex	1.0	0.35	2.8673	3.1012
	facet-facet	0.45	0.35	2.0219	3.1012
	vertex-facet	0.725	0.35	2.4446	3.1012
Octahedron - Tetrahedron	vertex-vertex	1.0	0.35	2.8545	3.0884
	facet-facet	0.45	0.35	1.7737	3.0884
	vertex(Oct)-facet(Tet)	0.725	0.45	2.1964	3.0884
	vertex(Tet)-facet(Oct)	0.725	0.45	2.4319	3.0884
Tetrahedron - Tetrahedron	vertex-vertex	1.0	0.35	2.8418	3.0757
	facet-facet	0.45	0.35	1.5254	3.0757
	vertex-facet	0.725	0.35	2.1836	3.0757

Table 5.10: Parameters for simulations of tetrahedron and octahedron used in co-crystallization simulations.

Binary mixture of octahedron and bitetrahedron					
Timestep			dt = 0.0005		
Parameters for potential					
aWCA					
	$\epsilon_{WCA,c}$	$\sigma_{WCA,0}$	$r_{WCA,0cut}$	$\sigma_{WCA,c}$	$r_{WCA,ccut}$
Octahedron - Octahedron	1.0	2.3094 - 2.3094	2.5922	0.8448	0.9482
Octahedron - Bitetrahedron	1.0	2.3094 - 1.5396	2.1602	0.8448	0.9482
Bitetrahedron - Bitetrahedron	1.0	1.5396 - 1.5396	1.7281	0.8448	0.9482
shifted-gaussian					
		ϵ_{sg}	σ_{sg}	r_0	$r_{sg,cut}$
Octahedron - Octahedron	vertex-vertex	1.0	0.35	2.9482	3.1821
	facet-facet	0.45	0.35	2.1029	3.1821
	vertex-facet	0.725	0.35	2.5256	3.1821
Octahedron - Bitetrahedron	vertex-vertex	1.0	0.35	2.8892	3.1231
	facet-facet	0.45	0.35	1.9338	3.1231
	vertex(Oct)-facet(Bit)	0.725	0.35	2.3564	3.1231
	vertex(Bit)-facet(Oct)	0.725	0.35	2.4666	3.1231
Bitetrahedron - Bitetrahedron	vertex-vertex	1.0	0.35	2.8303	3.0642
	facet-facet	0.45	0.35	1.7647	3.0642
	vertex-facet	0.725	0.35	2.2975	3.0642

Table 5.11: Parameters for simulations of bitetrahedron and octahedron used in co-crystallization simulations.

Binary mixture of octahedron and cuboctahedron					
Timestep			dt = 0.0005		
Parameters for potential					
aWCA					
	$\epsilon_{WCA,c}$	$\sigma_{WCA,0}$	$r_{WCA,0cut}$	$\sigma_{WCA,c}$	$r_{WCA,ccut}$
Octahedron - Octahedron	1.0	2.3094 - 2.3094	2.5922	0.667	0.7486
Octahedron - Cuboctahedron	1.0	2.3094 - 4.0	3.5410	0.667	0.7486
Cuboctahedron - Cuboctahedron	1.0	4.0 - 4.0	4.4898	0.667	0.7486
shifted-gaussian					
		ϵ_{sg}	σ_{sg}	r_0	$r_{sg,cut}$
Octahedron - Octahedron	vertex-vertex	1.0	0.35	2.7486	3.0141
	facet-facet	0.45	0.35	1.9033	3.0141
	vertex-facet	0.725	0.35	2.3259	3.0141
Octahedron - Cuboctahedron	vertex-vertex	1.0	0.35	2.7498	3.0153
	vertex(Cub)-facet(Oct)	0.725	0.35	2.3272	3.0153
	vertex(Oct)-Tfacet(Cub)	0.725	0.35	2.4566	3.0153
	vertex(Oct)-Sfacet(Cub)	0.547	0.35	2.4566	3.0153
	Tfacet(Cub)-facet(Oct)	0.45	0.35	2.0339	3.0153
	Sfacet(Cub)-facet(Oct)	0.272	0.35	2.0339	3.0153
Cuboctahedron - Cuboctahedron	vertex-vertex	1.0	0.35	2.7511	3.0166
	vertex-Tfacet	0.725	0.35	2.4578	3.0166
	vertex-Sfacet	0.547	0.35	2.4578	3.0166
	Tfacet-Tfacet	0.45	0.35	2.1646	3.0166
	Sfacet-Sfacet	0.095	0.35	2.1646	3.0166
	Sfacet-Tfacet	0.272	0.35	2.1646	3.0166
Note: For cuboctahedron, I set two different types of facet patches. Facet patch for triangle facet (Tfacet) and that for square facet (Sfacet).					

Table 5.12: Parameters for simulations of cuboctahedron and octahedron used in co-crystallization simulations.

Binary mixture of octahedron and decahedron					
Timestep			dt = 0.0005		
Parameters for potential					
aWCA					
	$\epsilon_{WCA,c}$	$\sigma_{WCA,0}$	$r_{WCA,0cut}$	$\sigma_{WCA,c}$	$r_{WCA,ccut}$
Octahedron - Octahedron	1.0	2.3094 - 2.3094	2.5922	0.75	0.8418
Octahedron - Decahedron	1.0	2.3094 - 2.3633	2.6225	0.75	0.8418
Decahedron - Decahedron	1.0	2.3633 - 2.3633	2.6527	0.75	0.8418
shifted-gaussian					
		ϵ_{sg}	σ_{sg}	r_0	$r_{sg,cut}$
Octahedron - Octahedron	vertex-vertex	1.0	0.40	2.8418	3.3128
	facet-facet	0.45	0.40	1.9965	3.3128
	vertex-facet	0.725	0.40	2.4192	3.3128
Octahedron - Decahedron	vertex-vertex	1.0	0.40	2.7859	3.2569
	facet-facet	0.45	0.40	1.9971	3.2569
	vertex(Oct)-facet(Dec)	0.725	0.40	2.4197	3.2569
	vertex(Dec)-facet(Oct)	0.725	0.40	2.3632	3.2569
Decahedron - Decahedron	vertex-vertex	1.0	0.40	2.7299	3.2009
	facet-facet	0.45	0.40	1.9976	3.2009
	vertex-facet	0.725	0.40	2.3637	3.2009

Table 5.13: Parameters for simulations of decahedron and octahedron used in co-crystallization simulations.

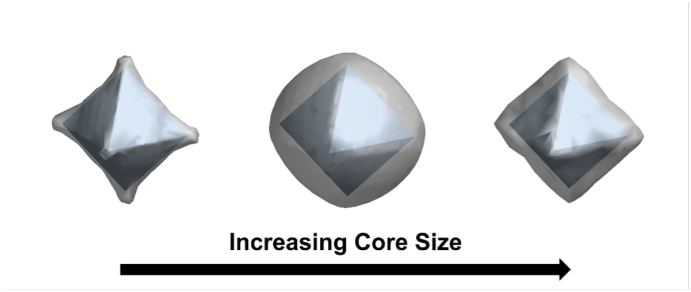

Figure 5.3: Spatial distribution of DNA ligand on the surface of octahedron nanocrystals. Thi Vo calculated the spatial distribution.

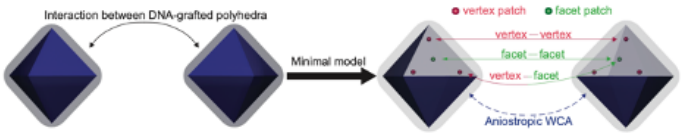

Figure 5.4: Minimal model for DNA-coated polyhedral NCs. Schematic diagram of minimal polyhedron nanocrystal model used in simulation. The polyhedron core and non-attractive DNA shell is modelled using the Anisotorpic WCA potential. The attractive interactions from DNA hybridization are included with patches distributed inside the polyhedron. In this model, two types of patches are used, i.e., the vertex type patch and facet type patch. Each patch interacts with all other patches via shifted-gaussian potential.

CHAPTER VI

Conclusions and Outlook

A spectacular variety of colloidal nanoparticles with different shapes and surface chemistries are now available for colloidal self-assembly. To make progress in the rational design of complex colloid assemblies, it is desirable to guide the experimental synthesis efforts by computational modelling. In this dissertation, I computationally study self-assembly processes that build stable complex architectures from colloidal nanoparticles.

6.1 Summary

In chapter 3, I investigated assembly of colloidal quasicrystals via Monte Carlo simulations of systems of hard tetrahedra. Using a pattern-recognition algorithm, I captured the temporal evolution of quasiperiodic arrangements, and elucidated the formation mechanism leading to complex quasiperiodic arrangements in colloidal systems. I also found that colloidal quasicrystals of hard tetrahedra exhibit nearly perfect quasiperiodic order, just like atomic quasicrystals. This result is of particular importance because colloidal superstructures with high quasiperiodic order can serve as scaffolds for photonic crystals with complete photonic bandgaps.

In chapter 4, I collaborated with Engel group at the University of Erlangen-Nuremberg to address stability of icosahedral quasicrystals in systems of model par-

ticles interacting via oscillating pair potential. Using free energy calculations in conjunction with phase transformation simulations, I quantitatively show thermodynamic stability of icosahedral quasicrystals against some rational approximants. I also investigated the transformation pathways leading to complex quasiperiodic arrangements.

In chapter 5, I collaborated with Chad Mirkin group at the Northwestern University to present a new DNA design, which offers ability to synthesize polyhedron packing from various polyhedron nanoparticles. Through a tightly coupled loop of simulation and experiment I have discovered remarkable complexity in the assembly of polyhedral nanoparticles. I have also investigated the co-crystallization of mixtures of different nanoparticle shapes, which offers a compelling platform to integrate functionality of distinct nanoparticles.

6.2 Outlook

Over the past two decades, the computational study of colloidal self-assembly has made strides. Molecular simulations have been efficiently predicting assembly behavior with sufficient accuracy and depicting thermodynamic stability of colloidal superstructures. The future for computational self-assembly simulations is filled with opportunities, and I propose two major directions for computational design of complex colloidal superstructures. The first direction that may propel the field of colloidal self-assembly is using inverse-engineering approaches for designing complex colloidal assemblies. Inverse-engineering approaches start from desired colloidal superstructure and then find the right building blocks for the self-assembly of the desired superstructure. A multitude of inverse-engineering approaches have been exploited to identify pair potentials or nanoparticle shapes for targeted self-assembly,

and some of the approaches have designed colloidal building blocks that can successfully form targeted materials including complex superstructures [83, 84]. I envision that these computational efforts will guide synthesis of nanoparticles capable of assembling into target complex superstructures. The second direction involves the development and applications of models for describing complex systems with greater accuracy. For colloidal building blocks with certain shapes, electrostatic charge, or surface chemistries, it is challenging to capture the realistic complexity of many-body interactions; considering interactions among all atoms in colloidal particles and suspending medium can be computationally expensive and limit the time scales accessible in simulations. Thus, extensive efforts must be devoted to developing coarse grained models that capture effective interparticle interactions and enable colloidal assembly within a reasonable computation time. Machine learning may play an important role here, by simplifying complex many-body interactions while reaching high prediction accuracy in colloid assemblies [85, 86].

6.3 Concluding Remarks

Nanoparticles with shapes or surface-bound ligands enable the design of selective interactions that expand opportunities to explore colloidal self-assembly at a higher level of complexity. My results contribute to understanding how complicated colloidal interactions conspires to generate a rich variety of complex superstructures. Resolving and understanding the assembly behavior would enable predictable control over low-cost and facile methods to synthesize stable functional nanomaterials. It is my hope that my dissertation work will provide the foundation for fabricating wholly new classes of materials with exciting properties, and to rationally predict the nanoparticles needed to realize them.

BIBLIOGRAPHY

BIBLIOGRAPHY

[1] A. Goldman and R. Kelton, "Quasicrystals and crystalline approximants," *Reviews of modern physics*, vol. 65, no. 1, p. 213, 1993.

[2] M. Engel, P. F. Damasceno, C. L. Phillips, and S. C. Glotzer, "Computational self-assembly of a one-component icosahedral quasicrystal," *Nature materials*, vol. 14, no. 1, pp. 109–116, 2015.

[3] M. Engel and H.-R. Trebin, "Self-assembly of monatomic complex crystals and quasicrystals with a double-well interaction potential," *Physical review letters*, vol. 98, no. 22, p. 225505, 2007.

[4] K. Je, S. Lee, E. G. Teich, M. Engel, and S. C. Glotzer, "Entropic formation of a thermodynamically stable colloidal quasicrystal with negligible phason strain," *Proceedings of the National Academy of Sciences*, vol. 118, no. 7, p. e2011799118, 2021.

[5] W. Cheng, M. J. Campolongo, J. J. Cha, S. J. Tan, C. C. Umbach, D. A. Muller, and D. Luo, "Free-standing nanoparticle superlattice sheets controlled by dna," *Nature materials*, vol. 8, no. 6, pp. 519–525, 2009.

[6] Y. Tian, J. R. Lhermitte, L. Bai, T. Vo, H. L. Xin, H. Li, R. Li, M. Fukuto, K. G. Yager, J. S. Kahn, *et al.*, "Ordered three-dimensional nanomaterials using dna-prescribed and valence-controlled material voxels," *Nature materials*, vol. 19, no. 7, pp. 789–796, 2020.

[7] N. Yazdani, M. Jansen, D. Bozyigit, W. M. Lin, S. Volk, O. Yarema, M. Yarema, F. Juranyi, S. D. Huber, and V. Wood, "Nanocrystal superlattices as phonon-engineered solids and acoustic metamaterials," *Nature communications*, vol. 10, no. 1, pp. 1–6, 2019.

[8] S.-H. Kim, S. Y. Lee, S.-M. Yang, and G.-R. Yi, "Self-assembled colloidal structures for photonics," *NPG Asia Materials*, vol. 3, no. 1, pp. 25–33, 2011.

[9] P. F. Damasceno, M. Engel, and S. C. Glotzer, "Predictive self-assembly of polyhedra into complex structures," *Science*, vol. 337, no. 6093, pp. 453–457, 2012.

[10] C. R. Laramy, M. N. O'Brien, and C. A. Mirkin, "Crystal engineering with dna," in *Spherical Nucleic Acids*, pp. 227–289, Jenny Stanford Publishing, 2020.

[11] H. Lin, S. Lee, L. Sun, M. Spellings, M. Engel, S. C. Glotzer, and C. A. Mirkin, "Clathrate colloidal crystals," *Science*, vol. 355, no. 6328, pp. 931–935, 2017.

[12] S. Wang, S. Lee, J. S. Du, B. E. Partridge, H. F. Cheng, W. Zhou, V. P. Dravid, B. Lee, S. C. Glotzer, and C. A. Mirkin, "The emergence of valency in colloidal crystals through electron equivalents," *Nature materials*, vol. 21, no. 5, pp. 580–587, 2022.

[13] S. Hajiw, B. Pansu, and J.-F. Sadoc, "Evidence for a c14 frank–kasper phase in one-size gold nanoparticle superlattices," *ACS nano*, vol. 9, no. 8, pp. 8116–8121, 2015.

[14] D. Shechtman, I. Blech, D. Gratias, and J. W. Cahn, "Metallic phase with long-range orientational order and no translational symmetry," *Physical review letters*, vol. 53, no. 20, p. 1951, 1984.

[15] K. Hayashida, T. Dotera, A. Takano, and Y. Matsushita, "Polymeric quasicrystal: Mesoscopic quasicrystalline tiling in abc star polymers," *Physical Review Letters*, vol. 98, no. 19, p. 195502, 2007.

[16] X. Ye, J. Chen, M. Eric Irrgang, M. Engel, A. Dong, S. C. Glotzer, and C. B. Murray, "Quasicrystalline nanocrystal superlattice with partial matching rules," *Nature materials*, vol. 16, no. 2, pp. 214–219, 2017.

[17] K. Nagao, T. Inuzuka, K. Nishimoto, and K. Edagawa, "Experimental observation of quasicrystal growth," *Physical review letters*, vol. 115, no. 7, p. 075501, 2015.

[18] M. Zoorob, M. Charlton, G. Parker, J. Baumberg, and M. Netti, "Complete photonic bandgaps in 12-fold symmetric quasicrystals," *Nature*, vol. 404, no. 6779, pp. 740–743, 2000.

[19] K. Kelton, "Quasicrystals: Structure and stability," *International materials reviews*, vol. 38, no. 3, pp. 105–137, 1993.

[20] A.-P. Tsai, ""back to the future"- an account discovery of stable quasicrystals," *Accounts of chemical research*, vol. 36, no. 1, pp. 31–38, 2003.

[21] A.-P. Tsai, "Discovery of stable icosahedral quasicrystals: progress in understanding structure and properties," *Chemical Society Reviews*, vol. 42, no. 12, pp. 5352–5365, 2013.

[22] N. Metropolis, A. W. Rosenbluth, M. N. Rosenbluth, A. H. Teller, and E. Teller, "Equation of state calculations by fast computing machines," *The journal of chemical physics*, vol. 21, no. 6, pp. 1087–1092, 1953.

[23] J. A. Anderson, M. E. Irrgang, and S. C. Glotzer, "Scalable metropolis monte carlo for simulation of hard shapes," *Computer Physics Communications*, vol. 204, pp. 21–30, 2016.

[24] J. A. Anderson, C. D. Lorenz, and A. Travesset, "General purpose molecular dynamics simulations fully implemented on graphics processing units," *Journal of computational physics*, vol. 227, no. 10, pp. 5342–5359, 2008.

[25] B. S. John, A. Stroock, and F. A. Escobedo, "Cubatic liquid-crystalline behavior in a system of hard cuboids," *The Journal of chemical physics*, vol. 120, no. 19, pp. 9383–9389, 2004.

[26] V. Ramasubramani, T. Vo, J. A. Anderson, and S. C. Glotzer, "A mean-field approach to simulating anisotropic particles," *The Journal of Chemical Physics*, vol. 153, no. 8, p. 084106, 2020.

[27] A. Yamamoto, "Crystallography of quasiperiodic crystals," *Acta Crystallographica Section A: Foundations of Crystallography*, vol. 52, no. 4, pp. 509–560, 1996.

[28] S. Walter and S. Deloudi, *Crystallography of quasicrystals: concepts, methods and structures*, vol. 126. Springer Science & Business Media, 2009.

[29] M. Paßens, V. Caciuc, N. Atodiresei, M. Feuerbacher, M. Moors, R. E. Dunin-Borkowski, S. Blügel, R. Waser, and S. Karthäuser, "Interface-driven formation of a two-dimensional dodecagonal fullerene quasicrystal," *Nature communications*, vol. 8, no. 1, pp. 1–7, 2017.

[30] S. J. Ahn, P. Moon, T.-H. Kim, H.-W. Kim, H.-C. Shin, E. H. Kim, H. W. Cha, S.-J. Kahng, P. Kim, M. Koshino, *et al.*, "Dirac electrons in a dodecagonal graphene quasicrystal," *Science*, vol. 361, no. 6404, pp. 782–786, 2018.

[31] S. Förster, K. Meinel, R. Hammer, M. Trautmann, and W. Widdra, "Quasicrystalline structure formation in a classical crystalline thin-film system," *Nature*, vol. 502, no. 7470, pp. 215–218, 2013.

[32] X. Zeng, G. Ungar, Y. Liu, V. Percec, A. E. Dulcey, and J. K. Hobbs, "Supramolecular dendritic liquid quasicrystals," *Nature*, vol. 428, no. 6979, pp. 157–160, 2004.

[33] S. Fischer, A. Exner, K. Zielske, J. Perlich, S. Deloudi, W. Steurer, P. Lindner, and S. Förster, "Colloidal quasicrystals with 12-fold and 18-fold diffraction symmetry," *Proceedings of the National Academy of Sciences*, vol. 108, no. 5, pp. 1810–1814, 2011.

[34] D. V. Talapin, E. V. Shevchenko, M. I. Bodnarchuk, X. Ye, J. Chen, and C. B. Murray, "Quasicrystalline order in self-assembled binary nanoparticle superlattices," *Nature*, vol. 461, no. 7266, pp. 964–967, 2009.

[35] C. Xiao, N. Fujita, K. Miyasaka, Y. Sakamoto, and O. Terasaki, "Dodecagonal tiling in mesoporous silica," *Nature*, vol. 487, no. 7407, pp. 349–353, 2012.

[36] Y. Sun, K. Ma, T. Kao, K. A. Spoth, H. Sai, D. Zhang, L. F. Kourkoutis, V. Elser, and U. Wiesner, "Formation pathways of mesoporous silica nanoparticles with dodecagonal tiling," *Nature communications*, vol. 8, no. 1, pp. 1–10, 2017.

[37] W. Steurer, "Quasicrystal structure and growth models: Discussion of the status quo and the still open questions," in *Journal of Physics: Conference Series*, vol. 809, p. 012001, IOP Publishing, 2017.

[38] W. Steurer, "Quasicrystals: What do we know? what do we want to know? what can we know?," *Acta Crystallographica Section A: Foundations and Advances*, vol. 74, no. 1, pp. 1–11, 2018.

[39] G. Y. Onoda, P. J. Steinhardt, D. P. DiVincenzo, and J. E. Socolar, "Growing perfect quasicrystals," *Physical review letters*, vol. 60, no. 25, p. 2653, 1988.

[40] F. Nori, M. Ronchetti, and V. Elser, "Strain accumulation in quasicrystalline solids," *Physical review letters*, vol. 61, no. 24, p. 2774, 1988.

[41] J. E. Socolar, T. Lubensky, and P. J. Steinhardt, "Phonons, phasons, and dislocations in quasicrystals," *Physical Review B*, vol. 34, no. 5, p. 3345, 1986.

[42] M. Feuerbacher, "Dislocations in icosahedral quasicrystals," *Chemical Society Reviews*, vol. 41, no. 20, pp. 6745–6759, 2012.

[43] T. Dotera, "Quasicrystals in soft matter," *Israel Journal of Chemistry*, vol. 51, no. 11-12, pp. 1197–1205, 2011.

[44] C. R. Iacovella, A. S. Keys, and S. C. Glotzer, "Self-assembly of soft-matter quasicrystals and their approximants," *Proceedings of the National Academy of Sciences*, vol. 108, no. 52, pp. 20935–20940, 2011.

[45] K. Barkan, H. Diamant, and R. Lifshitz, "Stability of quasicrystals composed of soft isotropic particles," *Physical Review B*, vol. 83, no. 17, p. 172201, 2011.

[46] S. Lee, E. G. Teich, M. Engel, and S. C. Glotzer, "Entropic colloidal crystallization pathways via fluid–fluid transitions and multidimensional prenucleation motifs," *Proceedings of the National Academy of Sciences*, vol. 116, no. 30, pp. 14843–14851, 2019.

[47] A. Haji-Akbari, M. Engel, A. S. Keys, X. Zheng, R. G. Petschek, P. Palffy-Muhoray, and S. C. Glotzer, "Disordered, quasicrystalline and crystalline phases of densely packed tetrahedra," *Nature*, vol. 462, no. 7274, pp. 773–777, 2009.

[48] A. Haji-Akbari, M. Engel, and S. C. Glotzer, "Phase diagram of hard tetrahedra," *The Journal of Chemical Physics*, vol. 135, no. 19, p. 194101, 2011.

[49] W. Steurer, "Structural phase transitions from and to the quasicrystalline state," *Acta Crystallographica Section A: Foundations of Crystallography*, vol. 61, no. 1, pp. 28–38, 2005.

[50] I. Han, J. T. McKeown, L. Tang, C.-Z. Wang, H. Parsamehr, Z. Xi, Y.-R. Lu, M. J. Kramer, and A. J. Shahani, "Dynamic observation of dendritic quasicrystal growth upon laser-induced solid-state transformation," *Physical Review Letters*, vol. 125, no. 19, p. 195503, 2020.

[51] K. Kelton, G. Lee, A. K. Gangopadhyay, R. Hyers, T. Rathz, J. Rogers, M. Robinson, and D. Robinson, "First x-ray scattering studies on electrostatically levitated metallic liquids: Demonstrated influence of local icosahedral order on the nucleation barrier," *Physical Review Letters*, vol. 90, no. 19, p. 195504, 2003.

[52] G. Lee, A. Gangopadhyay, T. Croat, T. Rathz, R. Hyers, J. Rogers, and K. Kelton, "Link between liquid structure and the nucleation barrier for icosahedral quasicrystal, polytetrahedral, and simple crystalline phases in ti- zr- ni alloys: Verification of frank's hypothesis," *Physical Review B*, vol. 72, no. 17, p. 174107, 2005.

[53] T. Dotera, T. Oshiro, and P. Ziherl, "Mosaic two-lengthscale quasicrystals," *Nature*, vol. 506, no. 7487, pp. 208–211, 2014.

[54] T. M. Gillard, S. Lee, and F. S. Bates, "Dodecagonal quasicrystalline order in a diblock copolymer melt," *Proceedings of the National Academy of Sciences*, vol. 113, no. 19, pp. 5167–5172, 2016.

[55] T. Ishimasa, S. Iwami, N. Sakaguchi, R. Oota, and M. Mihalkovič, "Phason space analysis and structure modelling of 100 å-scale dodecagonal quasicrystal in mn-based alloy," *Philosophical magazine*, vol. 95, no. 33, pp. 3745–3767, 2015.

[56] C. L. Henley, "Random tiling models," in *Quasicrystals: the state of the art*, pp. 429–524, World Scientific, 1991.

[57] A. Reinhardt, F. Romano, and J. P. Doye, "Computing phase diagrams for a quasicrystal-forming patchy-particle system," *Physical review letters*, vol. 110, no. 25, p. 255503, 2013.

[58] A. Kiselev, M. Engel, and H.-R. Trebin, "Confirmation of the random tiling hypothesis for a decagonal quasicrystal," *Physical Review Letters*, vol. 109, no. 22, p. 225502, 2012.

[59] H. Pattabhiraman, A. P. Gantapara, and M. Dijkstra, "On the stability of a quasicrystal and its crystalline approximant in a system of hard disks with a soft corona," *The Journal of chemical physics*, vol. 143, no. 16, p. 164905, 2015.

[60] Y. Nagaoka, H. Zhu, D. Eggert, and O. Chen, "Single-component quasicrystalline nanocrystal superlattices through flexible polygon tiling rule," *Science*, vol. 362, no. 6421, pp. 1396–1400, 2018.

[61] C. Achim, M. Schmiedeberg, and H. Löwen, "Growth modes of quasicrystals," *Physical Review Letters*, vol. 112, no. 25, p. 255501, 2014.

[62] Z. V. Vardeny, A. Nahata, and A. Agrawal, "Optics of photonic quasicrystals," *Nature photonics*, vol. 7, no. 3, pp. 177–187, 2013.

[63] J. Towns, T. Cockerill, M. Dahan, I. Foster, K. Gaither, A. Grimshaw, V. Hazlewood, S. Lathrop, D. Lifka, G. D. Peterson, *et al.*, "Xsede: accelerating scientific discovery," *Computing in science & engineering*, vol. 16, no. 5, pp. 62–74, 2014.

[64] V. Ramasubramani, B. D. Dice, E. S. Harper, M. P. Spellings, J. A. Anderson, and S. C. Glotzer, "freud: A software suite for high throughput analysis of particle simulation data," *Computer Physics Communications*, vol. 254, p. 107275, 2020.

[65] E. G. Noya, C. K. Wong, P. Llombart, and J. P. Doye, "How to design an icosahedral quasicrystal through directional bonding," *Nature*, vol. 596, no. 7872, pp. 367–371, 2021.

[66] A. Tao, P. Sinsermsuksakul, and P. Yang, "Tunable plasmonic lattices of silver nanocrystals," *Nature nanotechnology*, vol. 2, no. 7, pp. 435–440, 2007.

[67] M. He, J. P. Gales, É. Ducrot, Z. Gong, G.-R. Yi, S. Sacanna, and D. J. Pine, "Colloidal diamond," *Nature*, vol. 585, no. 7826, pp. 524–529, 2020.

[68] J. Gong, R. S. Newman, M. Engel, M. Zhao, F. Bian, S. C. Glotzer, and Z. Tang, "Shape-dependent ordering of gold nanocrystals into large-scale superlattices," *Nature communications*, vol. 8, no. 1, pp. 1–9, 2017.

[69] D. García-Lojo, E. Modin, S. Gómez-Graña, M. Impéror-Clerc, A. Chuvilin, I. Pastoriza-Santos, J. Pérez-Juste, D. Constantin, and C. Hamon, "Structure and formation kinetics of millimeter-size single domain supercrystals," *Advanced Functional Materials*, vol. 31, no. 27, p. 2101869, 2021.

[70] M. R. Jones, R. J. Macfarlane, B. Lee, J. Zhang, K. L. Young, A. J. Senesi, and C. A. Mirkin, "Dna-nanoparticle superlattices formed from anisotropic building blocks," *Nature materials*, vol. 9, no. 11, pp. 913–917, 2010.

[71] M. R. Jones, R. J. Macfarlane, A. E. Prigodich, P. C. Patel, and C. A. Mirkin, "Nanoparticle shape anisotropy dictates the collective behavior of surface-bound ligands," *Journal of the American Chemical Society*, vol. 133, no. 46, pp. 18865–18869, 2011.

[72] M. N. O'Brien, M. Girard, H.-X. Lin, J. A. Millan, M. Olvera de la Cruz, B. Lee, and C. A. Mirkin, "Exploring the zone of anisotropy and broken symmetries in dna-mediated nanoparticle crystallization," *Proceedings of the National Academy of Sciences*, vol. 113, no. 38, pp. 10485–10490, 2016.

[73] Y. Wang, L. Dai, Z. Ding, M. Ji, J. Liu, H. Xing, X. Liu, Y. Ke, C. Fan, P. Wang, *et al.*, "Dna origami single crystals with wulff shapes," *Nature communications*, vol. 12, no. 1, pp. 1–8, 2021.

[74] W. Liu, M. Tagawa, H. L. Xin, T. Wang, H. Emamy, H. Li, K. G. Yager, F. W. Starr, A. V. Tkachenko, and O. Gang, "Diamond family of nanoparticle superlattices," *Science*, vol. 351, no. 6273, pp. 582–586, 2016.

[75] F. Lu, T. Vo, Y. Zhang, A. Frenkel, K. G. Yager, S. Kumar, and O. Gang, "Unusual packing of soft-shelled nanocubes," *Science advances*, vol. 5, no. 5, p. eaaw2399, 2019.

[76] M. N. O'Brien, H.-X. Lin, M. Girard, M. Olvera de la Cruz, and C. A. Mirkin, "Programming colloidal crystal habit with anisotropic nanoparticle building blocks and dna bonds," *Journal of the American Chemical Society*, vol. 138, no. 44, pp. 14562–14565, 2016.

[77] R. V. Thaner, Y. Kim, T. I. Li, R. J. Macfarlane, S. T. Nguyen, M. Olvera de la Cruz, and C. A. Mirkin, "Entropy-driven crystallization behavior in dna-mediated nanoparticle assembly," *Nano letters*, vol. 15, no. 8, pp. 5545–5551, 2015.

[78] Y. Wang, Y. Wang, X. Zheng, É. Ducrot, J. S. Yodh, M. Weck, and D. J. Pine, "Crystallization of dna-coated colloids," *Nature communications*, vol. 6, no. 1, pp. 1–8, 2015.

[79] D. Nykypanchuk, M. M. Maye, D. Van Der Lelie, and O. Gang, "Dna-guided crystallization of colloidal nanoparticles," *Nature*, vol. 451, no. 7178, pp. 549–552, 2008.

[80] K. C. Elbert, T. Vo, N. M. Krook, W. Zygmunt, J. Park, K. G. Yager, R. J. Composto, S. C. Glotzer, and C. B. Murray, "Dendrimer ligand directed nanoplate assembly," *ACS nano*, vol. 13, no. 12, pp. 14241–14251, 2019.

[81] M. Wertheim, "Fluids with highly directional attractive forces. iii. multiple attraction sites," *Journal of statistical physics*, vol. 42, no. 3, pp. 459–476, 1986.

[82] W. Lechner and C. Dellago, "Accurate determination of crystal structures based on averaged local bond order parameters," *The Journal of chemical physics*, vol. 129, no. 11, p. 114707, 2008.

[83] G. van Anders, D. Klotsa, A. S. Karas, P. M. Dodd, and S. C. Glotzer, "Digital alchemy for materials design: Colloids and beyond," *ACS nano*, vol. 9, no. 10, pp. 9542–9553, 2015.

[84] Y. Geng, G. van Anders, P. M. Dodd, J. Dshemuchadse, and S. C. Glotzer, "Engineering entropy for the inverse design of colloidal crystals from hard shapes," *Science advances*, vol. 5, no. 7, p. eaaw0514, 2019.

[85] P. Friederich, F. Häse, J. Proppe, and A. Aspuru-Guzik, "Machine-learned potentials for next-generation matter simulations," *Nature Materials*, vol. 20, no. 6, pp. 750–761, 2021.

[86] G. Campos-Villalobos, E. Boattini, L. Filion, and M. Dijkstra, "Machine learning many-body potentials for colloidal systems," *The Journal of Chemical Physics*, vol. 155, no. 17, p. 174902, 2021.